Computation of drag crisis of a circular cylinder using Hybrid RANS-LES and URANS models

Sai Saketha Chandra Athkuri, M.R. Nived, R. Aswin, Vinayak Eswaran *

Department of Mechanical and Aerospace Engineering, Indian Institute of Technology Hyderabad, Telangana, 502285, India

ARTICLE INFO

ABSTRACT

Numerical simulation of flow past a circular cylinder across the "drag-crisis" region is extremely challenging for turbulence models because the boundary layer undergoes laminar–turbulent transition and variable-locus separation. We investigate the SA-DDES hybrid model along with two variants, namely, SA-kLES and SA-ILES, based on Spalart–Allmaras (SA) model, and include for comparison the SA-BCM transition and the SA-URANS models, for Re ranging from 50,000 to 5 million, using an in-house unstructured grid solver. All hybrid RANS-LES models produced clearly turbulent-like behavior, as evident from the Q-criterion, while the URANS models did not. A decline in the drag coefficient is noticed in all the turbulence models, but not the sharp decrease observed experimentally, with one exception: the SA-BCM transition model, which predicted the drag coefficients much closer to the experiments. The hybrid RANS-LES models outperformed the URANS SA-BCM model only in the fully turbulent trans-critical region and better represent the physics in the wake region for all Reynolds numbers studied. All the hybrid RANS-LES models produced similar results, suggesting comparatively equal performance in predicting separated flows. We believe that the performance of a hybrid model for mid-range Reynolds numbers will be greatly enhanced if the model is equipped to handle the laminar–turbulent transition.

1. Introduction

Determining the appropriate flow characteristics around bluff bodies plays a crucial role in determining forces on the body. This has various applications in many fields, including ocean and marine engineering. A typical example of a bluff body is a circular cylinder. Numerically capturing the flow physics past a circular cylinder with a smooth surface has been a challenging test case due to the fact that the flow separation is not fixed by the geometry of the object. In a square cylinder, the 90-degree bend at the corner of the square fixes the separation point. In contrast, in a circular cylinder, due to the smooth curvature of the object, the separation is determined by the nature of the boundary layer.

Depending on the Reynolds number, Roshko (1954) classified the flow regimes into four categories: (a) sub-critical ($Re < 2 \times 10^5$), (b) critical ($2 \times 10^5 < Re < 5 \times 10^5$), (c) super-critical ($5 \times 10^5 < Re < 5 \times 10^6$), and (d) trans-critical ($Re \geq 5 \times 10^6$). In the sub-critical regime, the contribution of the shear stresses to the overall drag is lower in comparison to the pressure (or form) drag as the flow separates at around 80 degrees (measured from the front stagnation point of the cylinder), preventing pressure recovery in the wake side. However, in

the critical regime, the boundary layer transitions to a fully turbulent one, thereby delaying the flow separation to around 120 degrees and thus reducing the pressure drag on the cylinder significantly. This phenomenon is known as the "drag crisis".

Many researchers have experimentally studied the drag-crisis phenomenon. Williamson (1996) summarized the flow instabilities according to different flow regimes. Skin-friction distribution and local pressure coefficients for a wide range of sub- and super-critical Re were measured by Achenbach (1968). Schewe (1983) studied the force fluctuations on a cylinder for sub- and trans-critical Reynolds numbers. Shih et al. (1993) measured the drag coefficient and Strouhal number up to $Re = 8 \times 10^6$. The region between sub- and super-critical regions was studied by Bearman (1969) and Farell and Blessmann (1983). The influence of inlet turbulence on the drag crisis was studied by Pfeil and Orth (1990). Cantwell and Coles (1983) extensively measured various quantities like Reynolds stresses and time-averaged velocities in the wake region. Wieselsberger (1922) studied the flow past the cylinder for sub-critical Reynolds numbers. Vortex shedding past a circular cylinder for $1.5 \times 10^5 < Re < 5 \times 10^5$ was investigated by Desai et al. (2020). For $Re = 1.4 \times 10^5$, Particle Image Velocimetry

* Corresponding author.
E-mail addresses: me14m16p000002@iith.ac.in (S.S.C. Athkuri), me16m18p000001@iith.ac.in (M.R. Nived), me19mtech01002@iith.ac.in (R. Aswin), eswar@iith.ac.in (V. Eswaran).

(PIV), stereoscopic PIV, and time-resolved PIV experiments were conducted by Perrin et al. (2007, 2008) to compare the mean and phase averaged values of turbulent quantities in the cylinder wake to the numerical results obtained from DES.

In previous numerical studies, flow past a circular cylinder was solved using techniques like Unsteady Reynolds-Averaged Navier–Stokes (URANS), Large Eddy Simulation (LES), and hybrid RANS-LES methods. URANS results did not predict the drag crisis, possibly due to their inability to predict the boundary layer transition (Vaz et al., 2007; Ye and Wan, 2017). Travin et al. (2000) performed simulations using a hybrid RANS-LES technique called Detached Eddy Simulation (DES) by assuming laminar separation (LS, which assumes a laminar inlet flow) for $Re = 5 \times 10^4$ and $Re = 1.4 \times 10^5$ and turbulent separation (TS, assuming a turbulent inlet) for $Re = 1.4 \times 10^5$ and $Re = 3 \times 10^6$. The drag coefficient and pressure coefficient of $Re = 1.4 \times 10^5$ using LS gave a better match in comparison to the experimental data, while TS largely under-predicted it. Significant disparities in the skin friction distribution were reported for $Re = 3 \times 10^6$. There are studies performed using hybrid RANS-LES simulations (Moussaed et al., 2014; Lakshmipathy and Girimaji, 2010; Pereira et al., 2018). For instance, Lakshmipathy and Girimaji (2010) simulated Partially Averaged Navier–Stokes (PANS) method for flow past a cylinder at $Re = 1.4 \times 10^5$; Pereira et al. (2018) simulated PANS for $Re = 3900$; Moussaed et al. (2014) combined the RANS model with variational multiscale LES and studied the problem for $Re = 1.4 \times 10^5$ and 1.25×10^6. There were also several LES studies of the problem. Breuer (2000) performed a detailed numerical investigation on the influence of the sub-grid scale (SGS) model and grid refinement on the quality of predicted results. One of his key findings is that the grid refinement did not necessarily provide a better match with the experiments. Another LES study by Catalano et al. (2003) for $Re = 5 \times 10^5$ and 10^6 showed encouraging results in predicting the local pressure coefficient. However, the computed skin-friction distribution had discrepancies similar to that of Travin et al. (2000). Two-dimensional simulations with no SGS model were performed by Singh and Mittal (2005). Although the trend in the drag crisis near the trans-critical regime is captured, the drag coefficients are highly over-predicted in the sub- and super-critical regimes. Recently, Rodríguez et al. (2015) performed LES simulation using the WALE model for $2.5 \times 10^5 < Re < 8.5 \times 10^5$ and captured the drag coefficient of the critical region satisfactorily. However, the performance of the WALE model in sub- and super-critical regimes is yet to be published. Kim (2006) simulated cylinder flow with LES for sub-critical $Re = 3000, 3900, 5000$ and 1.4×10^5. Lee and Yang (2017) also performed LES but only for $Re = 6.31 \times 10^4$, 1.26×10^5, and 2.52×10^5. Yeon et al. (2016) studied a wide range of Reynolds numbers from sub-critical to super-critical Reynolds numbers, with results over-predicting the drag coefficients in the high end of the sub-critical regime. Lloyd and James (2016) also performed a similar study where they also reported a drop in the drag coefficient in the critical region. A comprehensive picture of the drag crisis obtained from experiments and LES numerical studies (single data point studies are omitted here) is shown in Fig. 1.

In an LES simulation, the mesh should locally resolve 80% of the turbulent kinetic energy. This increases the mesh requirement enormously when compared to a RANS simulation. Choi A N and Moin (2011) estimated that the number of grid points in wall-resolved LES is one to three orders of magnitude greater than that in wall-modeled LES in the near-wall regions. This is evident from the simulations of Rodríguez et al. (2015) and Yeon et al. (2016): the control volumes in their meshes went as high as 100 million in the high sub-critical regime. The other LES simulations (Lee and Yang, 2017; Lloyd and James, 2016) also used meshes having 5–10 million elements for sub-critical Reynolds numbers. The mesh size can be reduced drastically by performing a hybrid RANS-LES simulation. For instance, Travin et al. (2000) used a mesh having only half a million cells; Vaz et al. (2007) and Moussaed et al. (2014) used meshes having 1.2 million

cells. This has motivated the present authors to perform hybrid RANS-LES simulations with meshes having 0.5–1 million cells while resolving 80% turbulent kinetic energy only in the wake region where the LES is used by the hybrid method. The use of unstructured meshes has aided in refining the grid in the areas of interest, thereby increasing the numerical accuracy of the scheme at a lower computational cost. We will also present a detailed study on the effect of grid refinement and hybrid models on finer grids.

There are many numerical studies that are constrained to a particular regime of the cylinder flow and a particular technique. The objective of this study is to investigate the performance of various turbulence models, namely, Spalart–Allmaras (SA)-URANS (Spalart and Allmaras, 1994; Eça et al., 2007) and three hybrid RANS-LES turbulence models (SA-DDES, SA-kLES and SA-ILES methods) for a wide range of Reynolds numbers ranging from 5×10^4 to 5×10^6. This study was undertaken to study the current capabilities of hybrid RANS-LES turbulence models in accurately simulating flows with strong separation features. We also simulate using the SA-BCM transition model (Çakmakçıoğlu et al., 2020) in comparison to other hybrid models to study the role of transition in the drag crisis. All the turbulence models mentioned here are implemented in an in-house solver developed for the purpose of simulating three-dimensional (3D) compressible flows in an unstructured mesh environment (Athkuri and Eswaran, 2020; Assam et al., 2018).

This paper is organized as follows: in Section 2, we describe the governing equations underlying compressible flows and the SA, SA-DDES, SA-kLES, SA-ILES, SA-BCM turbulence models. In Section 3, we discuss the case setup and the numerical settings used. In Section 4, we show the grid sensitivity study for the hybrid models. In Section 5, we discuss the effect of hybrid models on finer grids. Results of the drag crisis are presented in Section 6, with concluding remarks in Section 7.

2. Governing equations

The compressible form of Navier–Stokes (NS) equations is solved for simulating the flow past a circular cylinder. The vector integral form of the NS equations for an arbitrary control volume Ω enclosed by surface $d\Omega$ can be written as (Blazek, 2015):

$$\frac{\partial}{\partial t} \int_{\Omega} \mathbf{W} d\Omega + \oint_{d\Omega} (\mathbf{F_c} - \mathbf{F_v}) dS = 0, \tag{1}$$

where $\mathbf{W}$, $\mathbf{F_c}$ and $\mathbf{F_v}$ represent the vectors of conservative variables, convective fluxes, and viscous fluxes, respectively, given as:

$$\mathbf{W} = \begin{pmatrix} \rho \\ \rho u \\ \rho v \\ \rho w \\ \rho E \end{pmatrix}, \quad \mathbf{F_c} = \begin{pmatrix} \rho V \\ \rho u V + n_x p \\ \rho v V + n_y p \\ \rho w V + n_z p \\ \rho H V \end{pmatrix}, \quad \text{and} \quad \mathbf{F_v} = \begin{pmatrix} 0 \\ n_x \tau_{xx} + n_y \tau_{xy} + n_z \tau_{xz} \\ n_x \tau_{yx} + n_y \tau_{yy} + n_z \tau_{yz} \\ n_x \tau_{zx} + n_y \tau_{zy} + n_z \tau_{zz} \\ n_x \Theta_x + n_y \Theta_y + n_z \Theta_z \end{pmatrix}. \tag{2}$$

In Eq. (2), ρ is the density of the fluid; $u, v,$ and w are $x, y,$ and z components of velocity respectively; E and H are the total energy and total enthalpy of the fluid per unit mass and p is the pressure. Further, V is the contravariant velocity $(n_x u + n_y v + n_z w)$; $n_x, n_y,$ and n_z are the $x, y,$ and z components of the outward unit normal of the cell's face. The symbols Θ_x, Θ_y and Θ_z are given by,

$$\Theta_x = u\tau_{xx} + v\tau_{xy} + w\tau_{xz} + \hat{k}\frac{\partial T}{\partial x},$$
$$\Theta_y = u\tau_{yx} + v\tau_{yy} + w\tau_{yz} + \hat{k}\frac{\partial T}{\partial y}, \tag{3}$$
$$\Theta_z = u\tau_{zx} + v\tau_{zy} + w\tau_{zz} + \hat{k}\frac{\partial T}{\partial z},$$

where τ_{ij} is the stress tensor and $\hat{k}$ is the thermal conductivity of the fluid. In a turbulent simulation, except for density and pressure which are taken as Reynolds averaged quantities, all other flow variables in
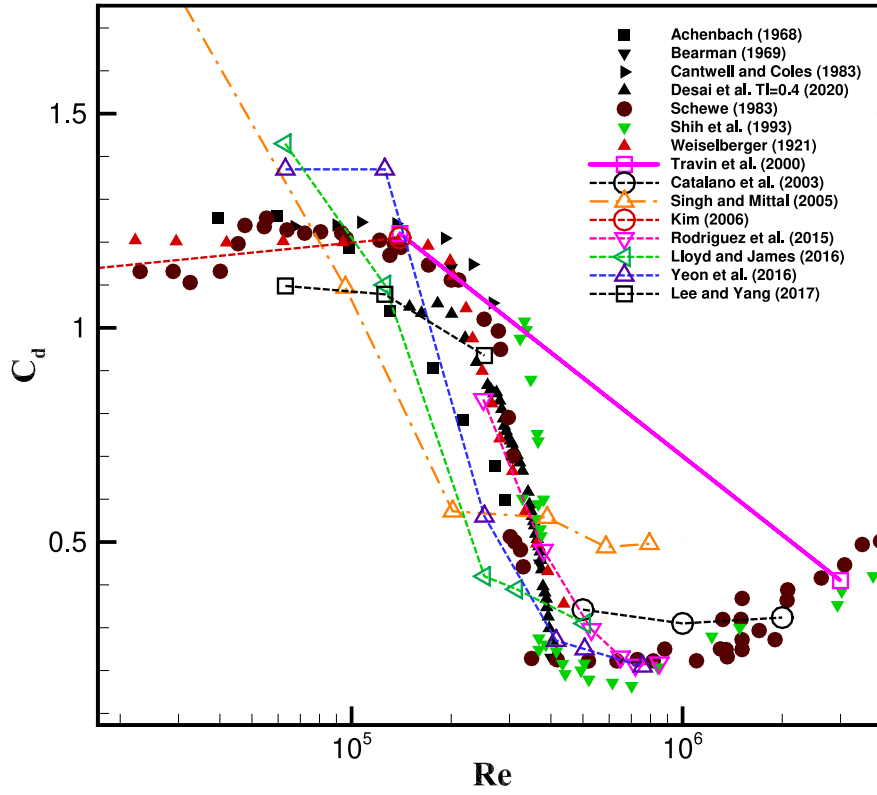
Fig. 1. Comprehensive summary of experimental (filled symbols) and numerical (LES) results in the drag-crisis problem.

Eqs. (1), (2) and (3) are Favre-averaged quantities. In Eq. (3), the stress tensor τ_{ij} is given by:

$$\tau_{ij} = \mu \left(\frac{\partial u_i}{\partial x_j} + \frac{\partial u_j}{\partial x_i} \right) - \frac{2}{3} \mu \delta_{ij} \left(\frac{\partial u_k}{\partial x_k} \right). \tag{4}$$

Assuming the Boussinesq approximation for turbulent flow, μ and $\hat{k}$ are given by:

$$\mu = \mu_L + \mu_T, \tag{5}$$

$$\hat{k} = \hat{k}_L + \hat{k}_T = c_p \left(\frac{\mu_L}{Pr_L} + \frac{\mu_T}{Pr_T} \right), \tag{6}$$

where μ_L and μ_T are laminar and turbulent dynamic viscosities wherein the latter depends on the choice of turbulence model; c_p is the specific heat coefficient at constant pressure, Pr_L is the laminar Prandtl number (0.72 for air), and Pr_T is the turbulent Prandtl number (here taken as 0.9). The laminar dynamic viscosity is given by the Sutherland formula,

$$\mu_L = \mu_0 \left(\frac{T}{T_0} \right)^{1.5} \left(\frac{T_0 + S}{T + S} \right), \tag{7}$$

where μ_0 is taken as 1.716×10^{-5} kg/ms, T_0 is 273.11 K, and S is 110.33 K.

2.1. Unsteady Reynolds Averaged Navier–Stokes (URANS) models

In this section, we briefly describe the URANS models employed in the study to investigate the drag crisis problem. The Spalart–Allmaras one-equation turbulence model and its transitional counterpart are described in this section.

2.1.1. Spalart–Allmaras model

We use the Spalart Allmaras-noft2 model (Spalart and Allmaras, 1994; Eça et al., 2007) as the base model in this study. We set f_{t2} as 0 in the original SA model to arrive at the SA-noft2 model (from here on, the

SA-noft2 model is referred to as the SA model). The transport equation for the eddy viscosity variable ($\tilde{v}$) reads:

$$\frac{\partial(\rho\tilde{v})}{\partial t} + \frac{\partial}{\partial x_j}(\rho\tilde{v}u_j) = P_{\tilde{v}} + \frac{1}{\sigma} \left\{ \frac{\partial}{\partial x_j} \left[(\mu_L + \rho\tilde{v}) \frac{\partial\tilde{v}}{\partial x_j} \right] + C_{b2}\rho \frac{\partial\tilde{v}}{\partial x_j} \frac{\partial\tilde{v}}{\partial x_j} \right\}$$
$$- C_{w1}f_w\rho \left(\frac{\tilde{v}}{d} \right)^2. \tag{8}$$

The terms on the right side of Eq. (8) correspond to the production ($P_{\tilde{v}}$), diffusion, and destruction, respectively. Further, d is the distance from the cell center to the nearest wall. The production term $P_{\tilde{v}}$ is:

$$P_{\tilde{v}} = C_{b1}\tilde{S}\rho\tilde{v}. \tag{9}$$

Now, the turbulent viscosity (μ_T^{SA}) is calculated as:

$$\mu_T^{SA} = \rho\tilde{v}f_{v1}; \quad f_{v1} = \frac{\chi^3}{\chi^3 + C_{v1}^3}; \quad \chi = \frac{\tilde{v}}{v_L}. \tag{10}$$

The term $\tilde{S}$ in Eq. (9) is given as:

$$\tilde{S} = \Omega + \frac{\tilde{v}}{\kappa^2 d^2} f_{v2}; \quad f_{v2} = 1 - \left(\frac{\chi}{1 + \chi f_{v1}} \right), \tag{11}$$

where Ω is the mean rotation rate magnitude (note that here, Ω is not the control volume) which is given by $\Omega = \sqrt{2\Omega_{ij}\Omega_{ij}}$, where Ω_{ij} is the rotation rate tensor. Further, f_w in Eq. (8) is given as:

$$f_w = g \left(\frac{1 + C_{w3}^6}{g^6 + C_{w3}^6} \right)^{\frac{1}{6}}; \quad g = r + C_{w2}(r^6 - r); \quad r = \frac{\tilde{v}}{\tilde{S}\kappa^2 d^2}. \tag{12}$$

The standard model constants are listed below.

| $C_{b1} = 0.1355$ | $C_{b2} = 0.622$ | | $C_{v1} = 7.1$ | $\kappa = 0.41$ |
| $\sigma = \frac{2}{3}$ | $C_{w1} = \frac{C_{b1}}{\kappa^2} + \frac{1+C_{b2}}{\sigma}$ | $C_{w2} = 0.3$ | $C_{w3} = 2$ |

The validation of the SA model implementation in the solver can be found in the works of Assam et al. (2018) and Joshi et al. (2019).

Table 1

Experimental and numerical conditions for the zero pressure gradient natural transition flat plate.

Case	Ma	Re_L	ν_T^{init}	$Tu_{\infty(\%)}$
Schubauer and Klebanoff (1955)	0.14	3.4×10^6	0.02	0.18
T3A (Savill, 1993)	–	3.7×10^5	0.02	3
T3B (Savill, 1993)	–	6.3×10^5	0.02	6

2.1.2. Spalart–Allmaras BCM transitional model

The SA-based transition model activates the production term ($P_{\tilde{\nu}}$) by checking for the onset transition location. This is achieved by comparing the locally computed momentum thickness Reynolds number (Re_θ) with the experimental critical momentum thickness Reynolds number (Re_{θ_c}). An intermittency function (γ_{BC}) is introduced for this purpose. The production term in Eq. (9) is modified to

$$P_{\tilde{\nu}}^{SABCM} = \gamma_{BC} C_{b1} \tilde{S} \rho \tilde{\nu}, \tag{13}$$

where γ_{BC} is the intermittency function.

The previous version of SA-BC (Spalart–Allmaras Bas–Cakmakcioglu) transitional model is not Galilean invariant (Cakmakcioglu et al., 2018). However, the intermittency function (γ_{BC}) was corrected to make it Galilean invariant to obtain the SA-BCM model (Çakmakçıoğlu et al., 2020), and we present the corrected form:

$$\gamma_{BC} = 1 - \exp\left(-\sqrt{Term_1} - \sqrt{Term_2}\right), \tag{14}$$

where $Term_1$ and $Term_2$ are:

$$Term_1 = \frac{\max(Re_\theta - Re_{\theta c}, 0.0)}{\chi_1 Re_{\theta c}}; \quad Term_2 = \max\left(\frac{\mu_T}{\chi_2 \mu_L}, 0.0\right), \tag{15}$$

where the momentum thickness Reynolds number (Re_θ) is given by:

$$Re_\theta = \frac{Re_\nu}{2.193}; \quad Re_\nu = \frac{d^2}{\nu_L} \Omega. \tag{16}$$

The critical momentum thickness Reynolds number (Re_{θ_c}) depends on the free stream turbulence intensity (Tu_∞) and is given as:

$$Re_{\theta c} = 803.73(Tu_\infty + 0.6067)^{-1.027}. \tag{17}$$

The constants χ_1 and χ_2 are 0.002 and 0.02, respectively. In the next section, we present the validation of the SA-BCM model in the solver.

2.1.3. Validation of SA-BCM model

To validate the implementation of the SA-BCM transition model in the solver, experiments conducted by Schubauer and Klebanoff (1955) for zero pressure gradient natural transition flat plate and the experiments of Savill (1993) (T3 A and T3B test cases) for bypass transition are used. The free-stream conditions for the flat plate are shown in Table 1.

Activation of the intermittency function results in a sudden increase in the skin-friction coefficient (C_f) at the transition location. The model is validated for three free-stream turbulence intensities (Tu_∞) for the flat plate. The skin-friction distribution along the plate for three cases are shown in Fig. 2. For the purpose of verification, the results of Çakmakçıoğlu et al. (2020) are also shown. The skin-friction coefficient matched well with the results of Çakmakçıoğlu et al. (2020) and with the experiments, thereby verifying and validating the SA-BCM model employed in the present solver.

In the next section, we introduce three hybrid RANS-LES models considered in this study.

2.2. Hybrid RANS-LES models

In this section, we describe the hybrid RANS-LES methods employed in this study to simulate flow past a circular cylinder with a smooth surface. The base model used in all the hybrid simulations is the SA (SA-noft2) model. Hence the role of SGS models can be studied systematically. The following hybrid models are investigated.

2.2.1. SA-DDES model

The Detached Eddy Simulation (DES) technique was first introduced by Spalart (1997). It is argued that by replacing the wall distance d with the cell dimension (Δ), the production and destruction terms in Eq. (8) balance each other, resulting in a Smagorinsky-type eddy viscosity. The Spalart–Allmaras - Delayed Detached Eddy Simulation (SA-DDES) method was later introduced (Spalart et al., 2006) to make DES resistant to ambiguous grid spacing and thus shield the turbulent boundary layer near the wall. The wall distance d is modified to $\tilde{d}$ as follows:

$$\tilde{d} = d - f_d \max\left(0, d - C_{DES}\Delta\right), \tag{18}$$

where Δ is the characteristic cell dimension (computed here as the cube root of cell volume), while the model constant C_{DES} is 0.65. Further, f_d is given by:

$$f_d = 1 - \tanh\left(\left[8r_d\right]^3\right), \tag{19}$$

where

$$r_d = \frac{\nu_L + \nu_T}{\sqrt{U_{ij} U_{ij}} \kappa^2 d^2}; \quad U_{ij} = \frac{\partial u_i}{\partial x_j}, \tag{20}$$

where ν_L and ν_T are laminar and turbulent kinematic viscosities, with the latter one being the solution obtained by solving the SA equation.

2.2.2. SA-kLES model

From Kolmogorov's theory of turbulence, the turbulent energy in larger scales is cascaded to smaller scales at a constant dissipation rate (ε). By determining the dissipation rate (ε) we can devise an SGS model which has a scaling proportional to $\Delta^{\frac{4}{3}}$, i.e.,

$$\nu_{SGS} = C_0 \varepsilon^{\frac{1}{3}} \Delta^{\frac{4}{3}}, \tag{21}$$

where C_0 is the model constant. This idea has been previously introduced by Wong and Lilly (1994) and has been pursued in the works of Carati et al. (2002). In their work, the dimensional quantity $C_0 \varepsilon^{\frac{1}{3}}$ is assumed to be insensitive to the grid filter width Δ and is determined in a dynamic fashion (Germano et al., 1991; Lilly, 1992). Later, De Langhe et al. (2005a,b) employed a similar expression for determining SGS eddy viscosity for Very Large Eddy Simulations (VLES) where they solved for an equation to determine the dissipation rate ε. However, the previous work used different turbulence models to estimate ε. In the present study, we estimate ε through the SA model, which is also being used for the RANS part of the hybrid RANS-LES formulations being discussed. However, the SA model does not directly provide the dissipation rate (ε), so we estimate the ε from the SA turbulent viscosity (ν_{SA}) and the strain rate magnitude (S) by the following expression

$$\varepsilon = \nu_{SA} S^2, \tag{22}$$

where S is $\sqrt{2S_{ij}S_{ij}}$ with strain rate tensor (S_{ij}) given by

$$S_{ij} = \frac{1}{2}\left(\frac{\partial u_i}{\partial x_j} + \frac{\partial u_j}{\partial x_i}\right). \tag{23}$$

Hence to obtain ε, the SA eddy viscosity equation has to be solved throughout the domain, not merely in the RANS-modeled region of the flow. The constant C_0 in Eq. (21) is taken as 0.068 as per the Ref. Sagaut (2006, p. 114). The SGS eddy viscosity (Eq. (21)) and the SA eddy viscosity (Eq. (10)) are then blended in a linear fashion by the parameter f_d in Eq. (19) to obtain the hybrid eddy viscosity as

$$\nu_{hybrid} = \nu_{SA} f_d + (1 - f_d)\nu_{SGS}. \tag{24}$$

The resulting hybrid eddy viscosity replaces μ_T/ρ in Eq. (6). We call this model the SA-kLES model, where the lower-case k serves to remind that the LES model uses Kolmogorov scaling and not the more common Smagorinsky model. The key difference between the SA-DDES and the SA-kLES formulations is that the length scale in DDES switches from wall distance to Δ and uses a Smagorinsky-type formula, whereas in
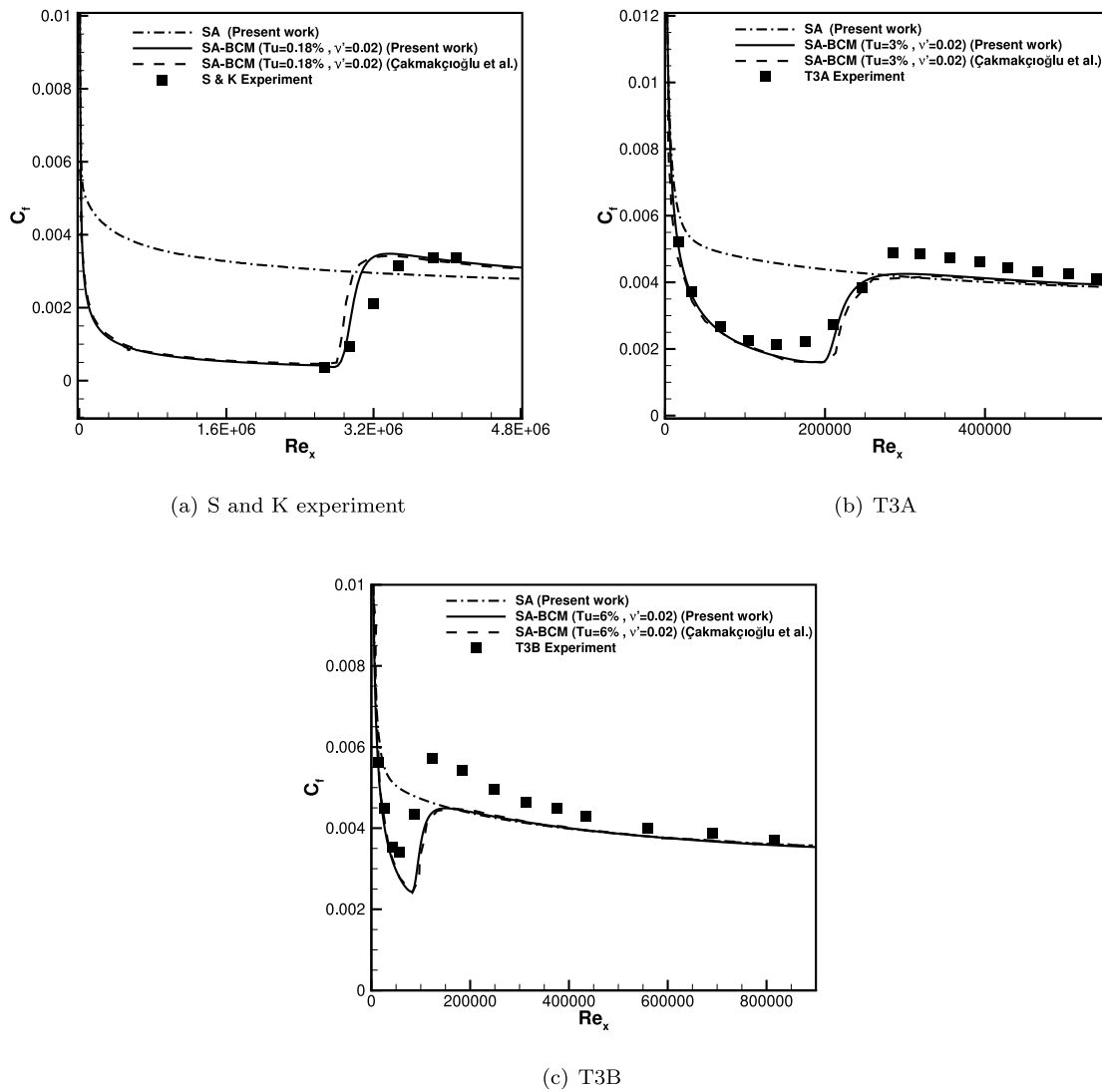
(a) S and K experiment

(b) T3A

(c) T3B

Fig. 2. Validation of SA-BCM model for zero pressure gradient flat plate; ν' is the inlet viscosity ratio initialized to activate the eddy viscosity in Eq. (8); Tu is the inlet turbulence; The x-axis is the local Reynolds number Re_x given by $\frac{\rho U_\infty x}{\mu_L}$. For the sake of completeness, the result of SA model is also shown.

the SA-kLES approach, the eddy viscosity changes from SA viscosity to SGS viscosity based on Eq. (21). Since the same parameter f_d (limiting RANS model to near wall region) is used to blend length scales and viscosities, with the base model unchanged, the effect of these two SGS models on the results like drag coefficient can be systematically investigated.

2.2.3. SA-ILES model

This model is inspired by the Implicit LES (ILES) approach. In an ILES method, no explicit SGS viscosity is added to the NS equations to capture the sub-grid scale eddies and their kinetic energy. Rather, it is left to the numerical dissipation to act for the turbulent dissipation in the flow. A similar line of thought is pursued in SA-ILES hybrid model, i.e., we use the SA model near the wall and no model (turbulent viscosity ν_T is set to 0) in the away regions. This was previously explored for the DES97 model (Islam and Thornber, 2016). However, here the term f_d in Eq. (19) is employed for a smooth transition from SA viscosity to laminar viscosity. The term f_d in Eq. (19) is employed to limit the SA viscosity to the near wall region. Hence the hybrid SA-ILES model eddy viscosity will be:

$$\nu_{hyb} = \nu_T^{SA} \times (1 - f_d). \tag{25}$$

3. Computational setup

In this section, we describe the numerical setup followed in the present study. We use an in-house solver to simulate the flow past a circular cylinder with a smooth surface, which uses an unstructured finite volume method to solve the compressible NS equations (Nived et al., 2022). The Spalart–Allmaras (SA) model in the solver has been extensively verified and validated from the data available in the NASA Turbulence Modeling Resource website (Resource, 2021) and has been used previously in the works of Assam et al. (2018), and Joshi et al. (2019). The following section presents the optimal meshes (different for each Re) employed in the drag crisis study. Before the drag crisis study, we performed a detailed grid sensitivity study with grids coarser and finer than the grid chosen as optimal. Also, we study the effect of hybrid models on the finer mesh.

3.1. Computational grids for the drag crisis simulations

In an LES simulation, performing a mesh independence study is impractical since the SGS eddy viscosity is directly dependent on the grid cell size Δ. However, it is a standard practice that the mesh should locally resolve at least up to 80% turbulent kinetic energy (Versión and Menter, 2012). To achieve this, the ratio of the integral length scale

Table 2
First wall spacing, number of cells in the spanwise direction, and grid sizes of the 'R' computational grids for varying Reynolds numbers.

Reynolds number (Re)	First wall spacing ($\times D$)	No. of cells in z (N_z)	Grid size
5×10^4	3×10^{-4}	24	519k
1.4×10^5	1×10^{-4}	26	543k
4.15×10^5	4×10^{-5}	28	809k
10^6	1.8×10^{-5}	28	853k
5×10^6	4×10^{-6}	28	962k
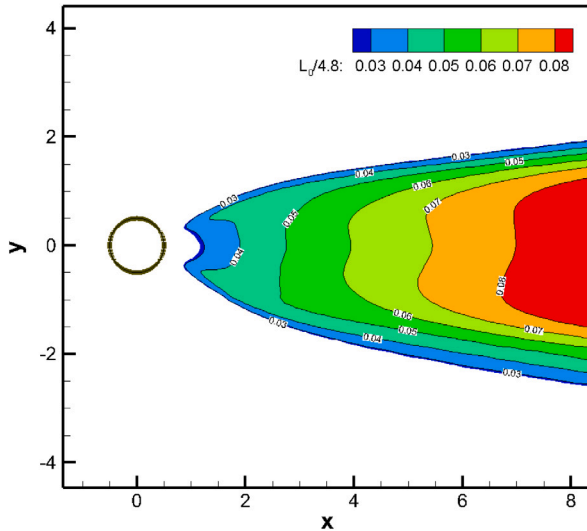
Fig. 3. The precursor SST $k - \omega$ simulation ($Re = 10^6$) to determine $L_0/4.8$ in the wake region.

(L_0) to the cell dimension Δ has to be greater than 4.8 as given by Pope (2001, chapter 6). So we need to ensure that the grid spacing Δ satisfies

$$\Delta \leqslant \frac{L_0}{4.8} \quad (26)$$

where the integral length scale is computed as $L_0 = \sqrt{k}/(0.09\omega)$ where k is the turbulent kinetic energy and ω is the specific dissipation rate. In Eq. (26), Δ is computed as the cube root of the cell volume. A pre-cursor 2D RANS (SST $k - \omega$) simulation is performed to determine the integral length scale. Fig. 3 shows the contours of $L_0/4.8$ obtained from this pre-cursor simulation. The computational grids used for the hybrid RANS-LES simulations are generated such that the grid $\Delta \leq L_0/4.8$ in the wake region of the cylinder, where the LES model will become operational in the hybrid calculations. The grid cells there are made hexahedral with equal sides (see Fig. 4).

The use of unstructured type meshes enables us to refine the grids locally to ensure Eq. (26) is satisfied. Five different meshes are created separately for each of the Reynolds numbers ($Re = 5 \times 10^4$, 1.4×10^5, 4.15×10^5, 10^6, and 5×10^6) used in this study. For each of these meshes, a separate $k - \omega$ precursor simulation was used to determine the optimal Δ in the wake. The immediate vicinity of the cylinder's wake (up to 2 times the diameter of the cylinder) has Δ values even finer than in the wake region. These five meshes are henceforth referred to as the 'R' meshes. In all the meshes, the circumference of the unit diameter ($D = 1$) cylinder has 201 grid points. The near-wall grid spacing is also decided based on the Reynolds number, and the non-dimensional distance of the first grid point is shown in Table 2. To create the 3D grids, the 2D grid on the cylinder is extruded in the third dimension to two times the diameter of the cylinder. The wake refinement starts from $2D$ to $10D$ downstream of the cylinder. The far-field boundary is situated at $50D$ units. The general structure of the R grid is shown in Fig. 4.

The non-dimensional distance (y^+) for the least and highest Re (50,000 and 5 million) is shown in Fig. 5 and is less than 1.5, as also is ensured for the other meshes. The cell dimension Δ in the wake region (extending up to $10D$ downstream of the cylinder) is taken as $0.09D$ for $Re = 50,000$ and $0.06D$ for $Re = 5$ million, compatible with Eq. (26). The simulations are all three-dimensional, as required in LES, with the symmetry condition imposed on the boundaries of the spanwise direction z. The domain aspect ratio (L_z/D) is chosen to be 2 with 24–28 planes in the spanwise direction, resulting in approximately cubic-shaped cells in the wake region. The value of $L_z = 2D$ has been used previously in the literature (Travin et al., 2000; Moussaed et al., 2014) to obtain reasonable predictions of flow over a circular cylinder for various Re. Higher domain aspect ratios also directly increase the computational expense per simulation, which has resulted in restricting it to $L_z/D = 2$.

3.2. Time-step

A second-order dual time-stepping algorithm is employed to solve the unsteady flow past the circular cylinder. The physical (outer loop) time-step (Δt) is determined by the Courant number such that the temporal error would not exceed the spatial error (Versión and Menter, 2012). However, as the algorithm is implicit, the Courant number restriction need not be applied strictly, i.e., being satisfied at all cells. Instead, a constant Δt is chosen, using data from a precursor SST $k - \omega$ simulation, such that the Courant number condition is satisfied in the wake region (where LES will be used). In conformity with the Courant condition for the strictest case, Δt is chosen to be 0.0005 s for all hybrid RANS-LES simulations. The number of inner loop iterations of the dual-time stepping is such that the residual of eddy viscosity ($\tilde{\nu}$) residual is allowed to reduce for more than two orders of magnitude in the inner loop, which requires approximately 20 inner iterations for marching each physical time-step.

3.3. Numerical setup

Although the flow is incompressible, as a compressible flow unstructured solver (with a Mach number of 0.2) is used in this work, the convective flux computation requires a differential treatment of upwind and downwind fluxes on the face. Second-order accuracy is achieved by employing the Circle Green–Gauss gradient method (Athkuri and Eswaran, 2020; Athkuri et al., 2022). The use of uniform cells in the wake region produces second-order accurate gradients and hence lower numerical diffusion in the area of interest. The laminar dynamic viscosity is obtained by the Sutherland formula (Eq. (7)). The free-stream temperature is 300 K, and the characteristic length is 1 m. Travin et al. (2000) followed a 'laminar separation' approach for $Re = 5 \times 10^4$ and 1.4×10^5 by initializing the flow field without feeding the turbulence from the inlet. Moussaed et al. (2014) performed hybrid simulations with 'turbulent separation' setup by including turbulence in the inlet flow. In the present work, we also investigate only the turbulent separation initiation where turbulence is fed from the inlet throughout the simulations. The reason for this is that, at the Reynolds numbers relevant to the drag crisis, the flow can be expected to be turbulent. Furthermore, the main purpose of this study is to check the models' performance under expected conditions (i.e. turbulent inlet) rather than fine-tune those conditions to obtain the 'best' results.
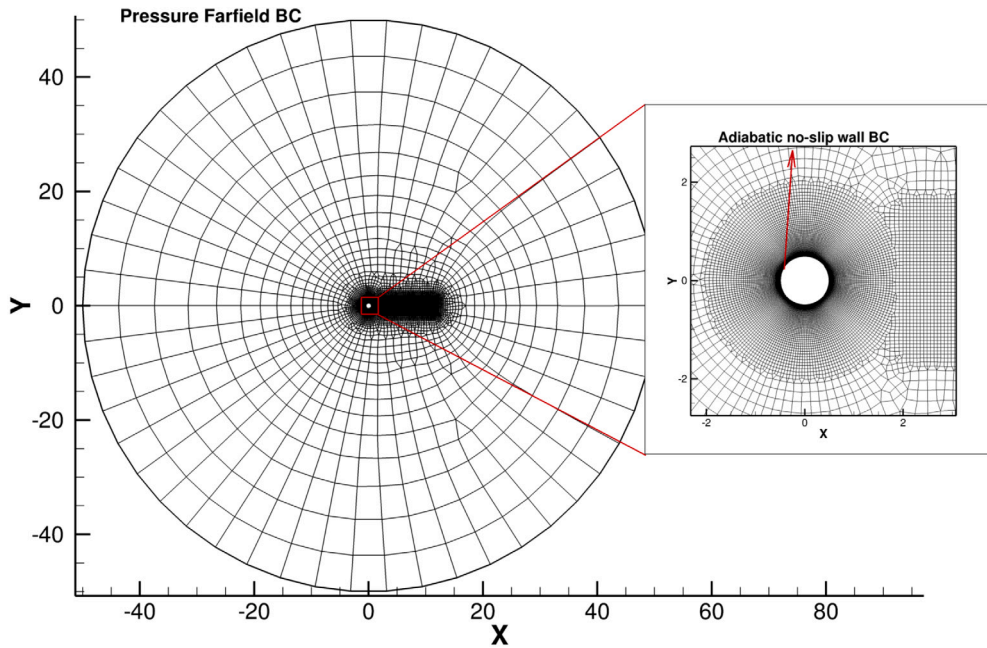
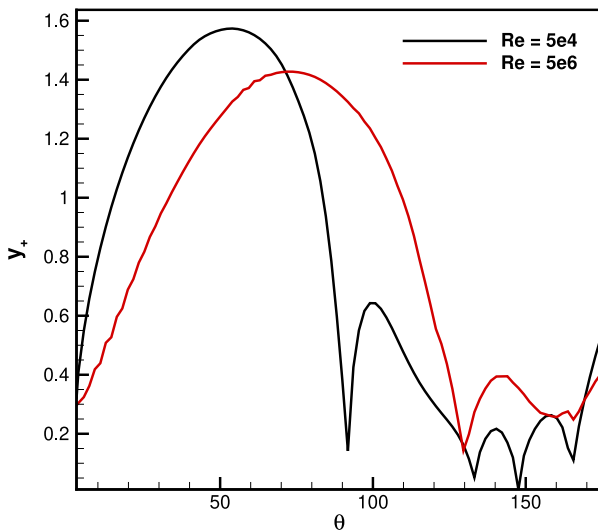**Fig. 4.** The common structure of the grid used in the circular cylinder computations.

Fig. 5. Non-dimensional distance ($y+$) on the cylinder.

The free-stream conditions and other solver settings are summarized in Table 3. In reference to the experiments (Schewe, 1983; Desai et al., 2020), Tu_∞ in SA-BCM simulations is taken as 0.4% with an initial viscosity ratio of 0.02. In this study, we do not explore the effect of free-stream turbulence intensity (Tu_∞) variation on the drag crisis problem.

All the simulations, both URANS and hybrid RANS-LES, have been performed with the same solver settings. Hence, this study should provide unambiguous results on the effect of different SGS models on flow predictions.

4. Grid sensitivity study

As discussed previously, a mesh independence study is not usually presented in LES simulation studies due to the fact that the SGS eddy viscosity is a function of grid cell size Δ. Following the standard practice that the mesh should locally resolve at least 80% turbulent kinetic energy (Versión and Menter, 2012), we have created 'R' grids, as explained in the previous section. Although we use these R meshes for the final simulations, we now also perform a grid sensitivity study with the SA-DDES model to study the effect of different grid resolutions. We study the role of the wake region's grid resolution on parameters like drag coefficient ($\overline{C_d}$), Strouhal number (St), and the base pressure coefficient (C_{pb}) at $\theta = \pi$ on the cylinder, and also the variation of the pressure coefficient with θ.

The SGS length-scale Δ plays a crucial role in determining the SGS eddy viscosity. The Δ value in a cell can be computed in several ways. The more popular ones are: first, by taking the maximum side length in a cell ($\max(\Delta x, \Delta y, \Delta z)$); second, by taking the cube-root of the cell volume ($vol^{1/3}$). Another scheme was proposed by Shur et al. (2015). In this work, we have taken Δ as the cube root of the cell volume.

The meshes used in this study are summarized in Table 4. We have considered three Δ values and a varying number of grid points on the cylinder. These mesh resolutions are comparable to that used by Travin et al. (2000) and Moussaed et al. (2014). Travin et al. (2000) performed grid sensitivity study with $\Delta = 0.048$ and 0.068, with results being clearly sensitive to the Δ chosen. Moussaed et al. (2014) performed the same with $\Delta = 0.1$ and $\Delta = 0.05$.

We now perform simulations on four separate new grids for $Re = 1.4 \times 10^5$ (**G1**, **G2**, **G4**, **G6**) with the SA-DDES model (numerical setup is discussed in Section 3.3). Of these, **G2**, **G4** and **G6** satisfy the criterion of Eq. (26), while **G1** is coarser than allowed by the criterion ($\Delta = 0.15$, compared to $\Delta \leq 0.09$) in the wake region. However, **G6** is also somewhat coarser in the non-wake region, having only 151 points on the cylinder surface (like **G1**) compared to 201 points for **G2** and **G4**. The number of cells in **G1**, **G2**, **G4**, **G6** are respectively 230,000, 540,000, 1.7M, and 500,000. We report the time-averaged drag coefficient, cylinder's base pressure, and Strouhal number obtained on these meshes in Table 4.

The meshes **G1**, **G2** and **G6** give comparatively close values for these quantities, which is evidence, as the meshes are roughly comparable in size (230k–500k cells), of the consistency of the simulations. However, the finest mesh G4 (1.7M cells) yields somewhat lower values for $\overline{C_d}$ and C_{pb}, indicating a possible grid-size effect on the simulations. That grid refinement produces a decrease in $\overline{C_d}$ has been reported by many researchers (Travin et al., 2000; Moussaed et al., 2014; Lo et al., 2005; Breuer, 2000). However, the results of all the **G** meshes are within the

Table 3

Solver settings followed in the simulations.

Flow conditions/Solver settings	Value/Method
Mach number (Ma)	0.2
Temperature (T)	300 K
Dynamic viscosity (μ)	$1.846 \times 10^{-5}\ \frac{kg}{ms}$
Characteristic length (L)	1 m
Turbulent Prandtl number	0.9
$\frac{\hat{v}}{v_L}$ (except SA-BCM)	5
$\frac{\hat{v}}{v_L}, Tu_\infty$ (for SA-BCM)	0.02, 0.4%
Gradient scheme	Circle Green–Gauss (CGG) method (Athkuri and Eswaran, 2020; Athkuri et al., 2022)
Time-stepping	Second-order implicit dual time-stepping (Weiss et al., 1999; Chandra, 2022)

Table 4

Results of grid sensitivity study performed with DDES model for $Re = 1.4 \times 10^5$ unless specified. The simulations here use $\Delta = vol^{1/3}$. The DES of Travin et al. (2000) was done with $\Delta = \max(\Delta x, \Delta y, \Delta z)$.

Grids	N_c	Δ	N_{cv}	$\overline{C_d}$	$-C_{pb}$	St
G1	151	0.15	230k	0.757	1.029	0.250
G2	201	0.09	540k	0.744	0.926	0.261
G4	201	0.05	1.7M	0.671	0.786	0.265
G6	151	0.09	500k	0.741	0.982	0.257
HRLES ($Re = 10^5$) (Hodara and Smith, 2017)	256	–	9.6M	0.76	–	–
DES (B1-4 (Lo et al., 2005))	100–240	–	0.42–0.96M	0.62–0.704	0.83–0.91	0.287–0.305
SST DES (Lakshmipathy and Togiti, 2011)	–	–	2M	0.847	0.892	0.26
DES (TS 2 (Travin et al., 2000))	150	0.05	680k	0.59	0.67	0.31
DES (TS 4 (Travin et al., 2000))	118	0.07	370k	0.64	0.7	0.28
Roshko (1961) ($Re > 3.6 \times 10^6$)	–	–	–	0.62–0.74	0.85	0.27
Achenbach (1968) (3.6×10^6)	–	–	–	0.76	0.85	0.27

range of values obtained by other hybrid RANS-LES results by previous authors, also shown in Table 4.

We have also included experimental data from Roshko (1961) and Achenbach (1968) in Table 4, which have $\overline{C_d}$, C_{pb} and St values that compare well with our simulation results. However, these data are for $Re = 3.6 \times 10^6$ while our simulations were for $Re = 1.4 \times 10^5$. This suggests that the present SA-DDES and other RANS-LES models in Table 4 at $Re = 1.4 \times 10^5$ are actually simulating the flow with post-crisis fully turbulent boundary layer, which is seen experimentally at 3.6×10^6. This suggests these models will not capture the drag crisis because they cannot simulate the laminar–turbulent boundary layer transition.

Consider Fig. 6 that shows the coefficient of pressure C_p vs. θ for the $Re = 1.4 \times 10^5$ case on the grids **G1**, **G2**, **G4** and **G6**. We have included the numerical data of Travin et al. (2000) for their 'turbulent separation' case. We also show the high Re results of Roshko (1961), James et al. (1980) and Achenbach (1968). The C_p profile obtained on the **G1**, **G2**, **G4** and **G6** meshes fall within the experimental data as does the numerical result of Travin et al. (2000). In fact, the match with the experiments is very good. These results reinforce the suggestions made above that the hybrid RANS-LES models are actually simulating the higher Re post-crisis flow field because they lack a mechanism for the laminar–turbulent transition.

The plots of Q-criterion colored by viscosity ratio obtained from simulations performed on **G1**, **G2**, and **G4** grids are shown in Fig. 7. As we can see, the coarsest mesh **G1** clearly produced two-dimensional vortical structures, while **G2** and **G4** produced turbulent three-dimensional vortical structures. The finest mesh **G4** has a better Q-criterion qualitatively. This seems to suggest that while the criterion specified by Eq. (26) is adequate, it may be bettered by using an even smaller grid interval. The **G2** mesh is chosen to perform simulations of drag crisis at $Re = 1.4 \times 10^5$ (in Section 6) as it has 201 points on the cylinder and is finer enough in the wake to resolve at least 80% turbulent kinetic energy. The finer **G4** mesh having 1.7 million cells is used to study the effect of various hybrid models in predicting the drag and Strouhal number for the same Re in the next section.

The conclusion that can be drawn from all of the above is that the SA-DDES hybrid RANS model does not capture the drag crisis because
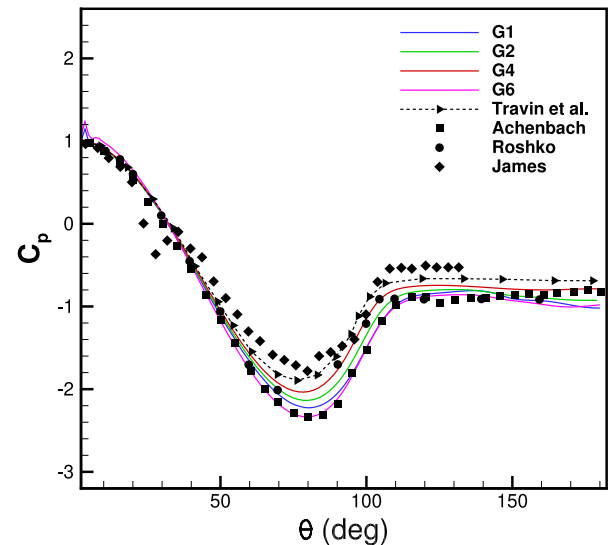

Fig. 6. Variation of mean pressure coefficient along the cylinder computed for $Re = 1.4 \times 10^5$ compared with experimental data of James et al. (1980) ($Re = 3.8 \times 10^6$), Achenbach (1968) ($Re = 3.6 \times 10^6$), Roshko (1961) ($Re = 8.4 \times 10^6$) and numerical results of Travin et al. (2000) (TS2).

it lacks a laminar–turbulent transition mechanism. We will see that this is also true of the other two hybrid models considered in this study.

5. Comparison of the three hybrid models

We have simulated SA-DDES, SA-kLES, and SA-ILES on the **G4** grid. The simulations are performed for more than 25 shedding cycles. The values of $\overline{C_d}$, C_{pb}, and St obtained for the three models are shown in Table 5. The results are remarkably close, suggesting almost no difference in the quantitative predictions. The Q-criterion (colored by
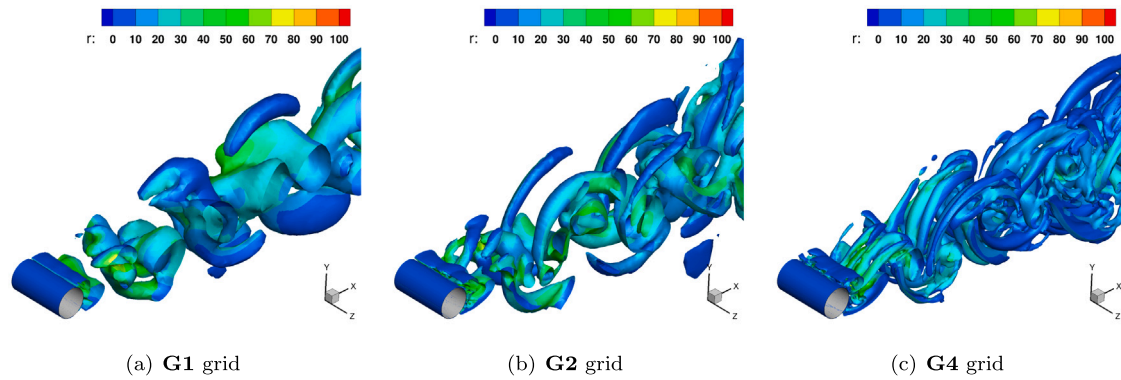
(a) **G1** grid   (b) **G2** grid   (c) **G4** grid

Fig. 7. Q-criterion ($= 0.5 \frac{1}{s^2}$) colored by viscosity ratio r ($= \nu_t/\nu$). Here, the blue color denotes a ratio of 0 or less, and red denotes a ratio of 100.
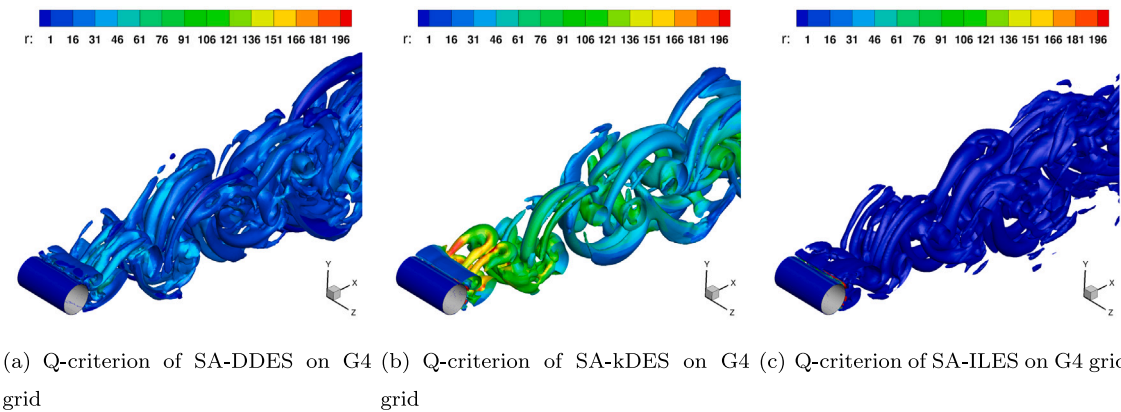

(a) Q-criterion of SA-DDES on G4 grid   (b) Q-criterion of SA-kDES on G4 grid   (c) Q-criterion of SA-ILES on G4 grid

Fig. 8. Q-criterion ($= 0.5 \frac{1}{s^2}$) colored by viscosity ratio r ($= \nu_t/\nu$) for SA-DDES, SA-kLES and SA-ILES models. The blue color of viscosity ratio r denotes 1 and red denotes 196.

Table 5
Effect of hybrid models.

Hybrid models	N_c	Δ	N_{cv}	$\overline{C_d}$	$-C_{pb}$	St
SA-DDES	201	0.05	1.7M	0.671	0.786	0.265
SA-kLES	201	0.05	1.7M	0.668	0.799	0.263
SA-ILES	201	0.05	1.7M	0.683	0.798	0.268

viscosity ratio $= \nu_{SGS}/\nu_L$) produced by the SA-DDES, SA-kLES, and SA-ILES is shown in Fig. 8. We can conclude that qualitatively all three models show turbulent-like vortical structures in the wake. However, the magnitudes of the eddy viscosity ratio r ($= \nu_t/\nu$) differ significantly for all the three hybrid models. The SA-kLES model is observed to have a higher value of r in the wake region away from the cylinder as it uses a different subgrid model (Eq. (21)) compared to the Smagorinsky model in SA-DDES. In SA-ILES, the value of r remains unity except for a small region very close to the cylinder, as there is no LES subgrid model used in the away wall regions, as given by Eq. (25). The intermittent nature in the evolution of C_d and C_l plotted in Fig. 9 suggests that all the three models produce similar random unsteady turbulent-like behavior.

The pressure coefficient profiles for the case of $Re = 1.4 \times 10^5$ are shown in Fig. 10. We see that the three models' results match closely with each other and also with high Re experiments in the transcritical regime. For the case of $Re = 10^6$, shown in Fig. 11, we see that the SA-ILES profile is somewhat different from those of SA-DDES and SA-kLES which are again identical. Surprisingly, the profile of the SA-ILES model matches excellently with that from the high Re experiments and with that of Travin et al. (2000) more than the other two models. As seen before, all three models do not match with the experiments of the approximately same Reynolds numbers (850k, 1.2M), the probable reason for which has been discussed above.

All the coefficients, Q-criterion, and the C_p profiles suggest that the SA-DDES and SA-kLES give almost identical results, while the SA-ILES gives close but not identical results. The SA-DDES and SA-kLES models have non-zero turbulent viscosity, while the SA-ILES does not. The turbulent viscosities in SA, SA-DDES, and SA-kLES increase with Re due to increased turbulent production. However, in the SA-ILES model, there is no external turbulent viscosity to account for the increase in Re. Hence the model is largely insensitive to Re. This can be seen from Fig. 12 where the pressure coefficient variation of the SA-ILES model (simulated on the 'R' meshes) along the cylinder for $Re = 5 \times 10^4$, 1.4×10^5, 4.15×10^5, and 10^6 is compared with high Re experiments. For $Re = 1.4 \times 10^5$, 4.15×10^5, and 10^6, the SA-ILES model is almost insensitive to Re and matched well with numerical data of Travin et al. (2000) and high Re experiments of Roshko (1961) and James et al. (1980). The differences in the wake region pressure coefficient are mainly due to the SA model that is employed in the close proximity of the cylinder.

6. Results of drag crisis simulations

In this section, we present the results of the simulations with all the turbulence models discussed in Section 2.2 over the range of Reynolds numbers of the drag crisis. We have used separate meshes for each Re, as discussed in Section 3.1. The meshes all meet the criteria of resolving 80% turbulent kinetic energy and produce three-dimensional vortical structures for the Q-criterion in the LES zones in the wake of the cylinder.

Our analysis will be mainly focused on comparing, across the entire range of Reynolds numbers, important flow features like drag coefficient, base pressure coefficient, pressure distribution, and flow separation angle along the cylinder's azimuth. Each simulation is performed
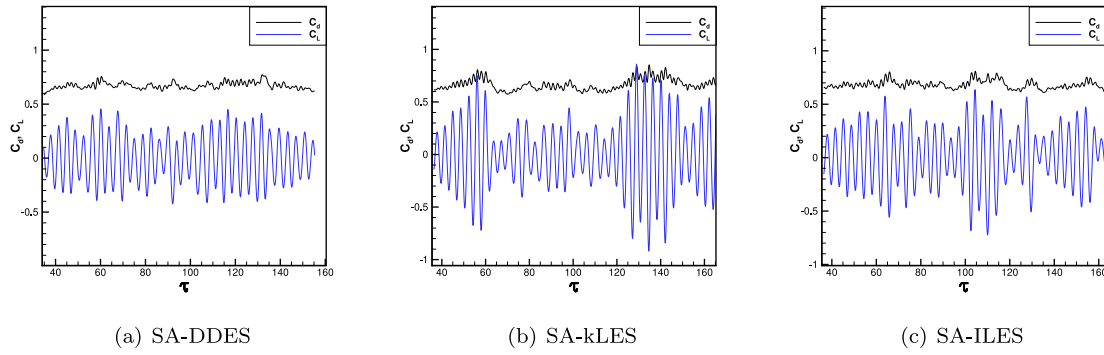
(a) SA-DDES

(b) SA-kLES

(c) SA-ILES

Fig. 9. Evolution of drag and lift coefficients with non-dimensional time ($\tau = \frac{tU}{D}$) using the hybrid models on fine grid **G4**.
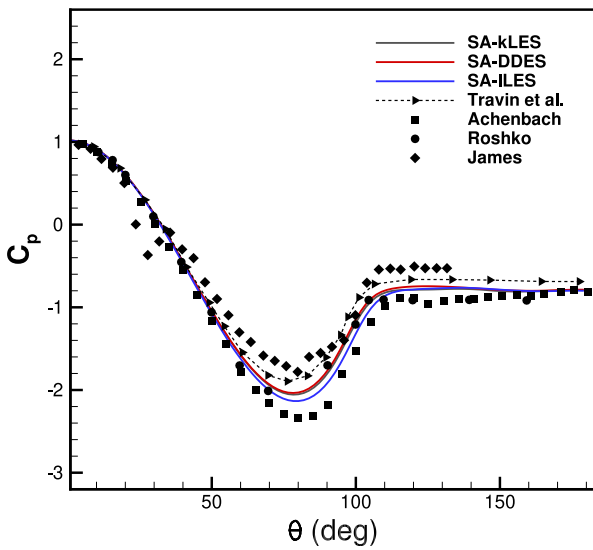

Fig. 10. Comparison of pressure profiles at $Re = 1.4 \times 10^5$ of SA-DDES, SA-kLES, SA-ILES models with experiments data of James et al. (1980) ($Re = 3.8 \times 10^6$), Achenbach (1968) ($Re = 3.6 \times 10^6$), Roshko (1961) ($Re = 8.4 \times 10^6$) and numerical results of Travin et al. (2000) (TS2).
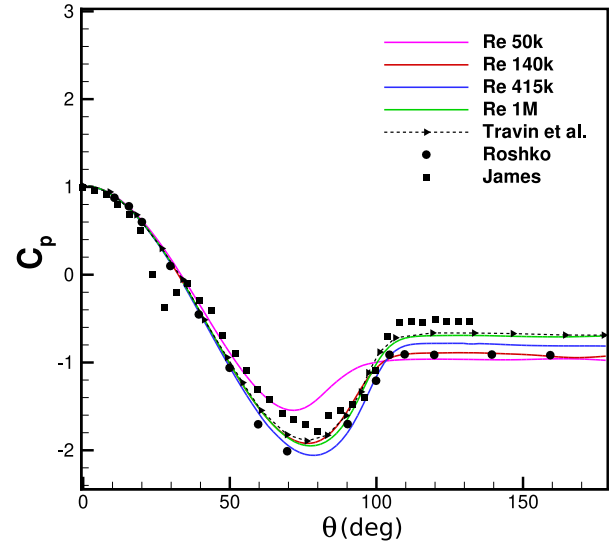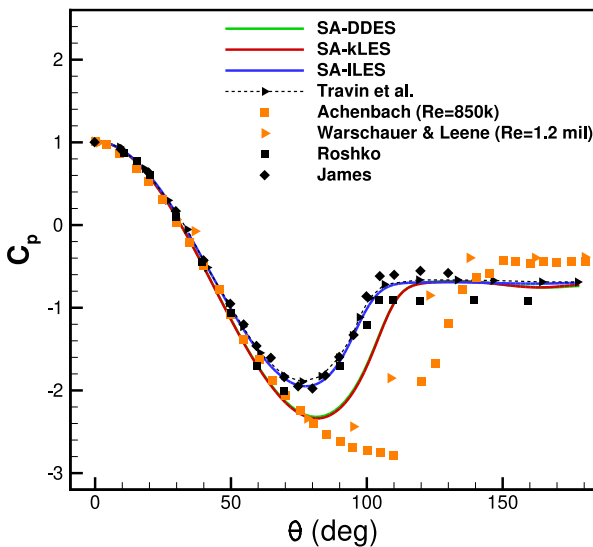

Fig. 12. Variation of mean pressure coefficient along the cylinder computed with SA-ILES model for the Re across the drag crisis compared with experimental data of James et al. (1980) ($Re = 3.8 \times 10^6$), Achenbach (1968) ($Re = 3.6 \times 10^6$), Roshko (1961) ($Re = 8.4 \times 10^6$) and numerical results of Travin et al. (2000) (TS2).

Fig. 11. Comparison of pressure profiles at $Re = 10^6$ of SA-DDES, SA-kLES, SA-ILES models and Travin et al. (2000) (TS2) with experiments data of James et al. (1980) ($Re = 3.8 \times 10^6$), Achenbach (1968) ($Re = 3.6 \times 10^6$, 8.5×10^6), Roshko (1961) ($Re = 8.4 \times 10^6$), Warschauer and Leene (1971) ($Re = 1.2 \times 10^6$).

for more than 20 shedding cycles. The average values reported are averaged over the 20 shedding cycles after the "dynamic steady-state" is achieved in the simulation.

Consider the flow over the cylinder for $Re = 5 \times 10^4$. The time-dependent drag and lift coefficients for all the models are shown in Fig. 13. The SA and SA-BCM URANS models predict very similar C_D and C_L that lack intermittent behavior. On the other hand, a strong intermittent behavior is evident from the C_L plots of all the hybrid RANS-LES simulations. Despite their intermittent behavior, their time-averaged drag coefficients are only slightly different from each other. This is observed for other Reynolds numbers also.

The experimental data on recirculation length for critical and super-critical Re is limited in the literature, so we do not compare the recirculation length.

The Q-criterion (see Fig. 14) also suggest more turbulence-like behavior in the hybrid models than in the URANS models. Two-dimensional vortical structures are dominantly seen in the URANS models (SA and SA-BCM), while the hybrid models produced three-dimensional vortical structures in the wake. It is worthy of note that SA-DDES and SA-ILES models produced similar vortical structures in the wake, while the SA-kLES model had a mixture of two-dimensional and three-dimensional structures. This can possibly be attributed to the fact that ν_{SGS} ($= C_0(\nu_{SA})^{\frac{1}{3}}(S\Delta^2)^{\frac{2}{3}}$) of the SA-kLES model depends on both the SA eddy viscosity and the Smagorinsky type SGS viscosity.
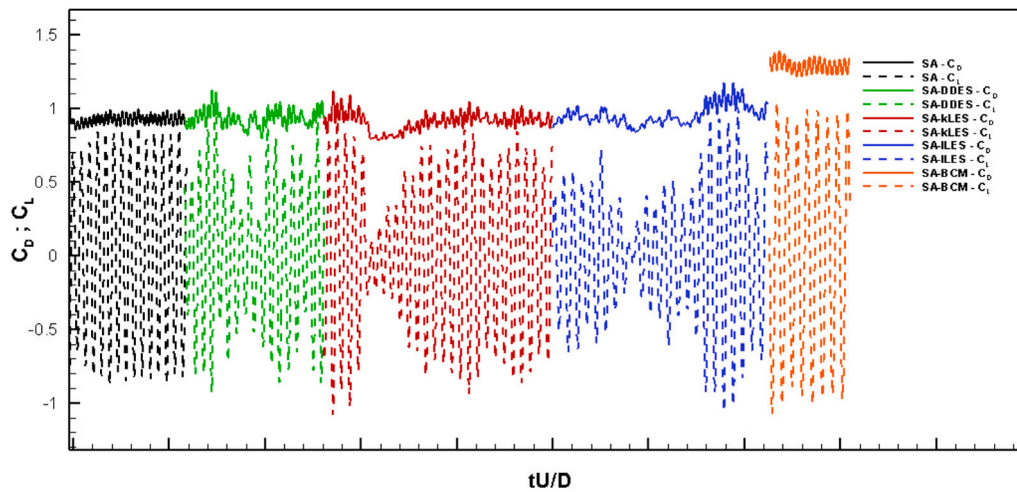
Fig. 13. Time dependent parameters for cylinder flow $Re = 5 \times 10^4$; upper curve —C_D, lower curve —C_L.

(a) SA

(b) SA-BCM
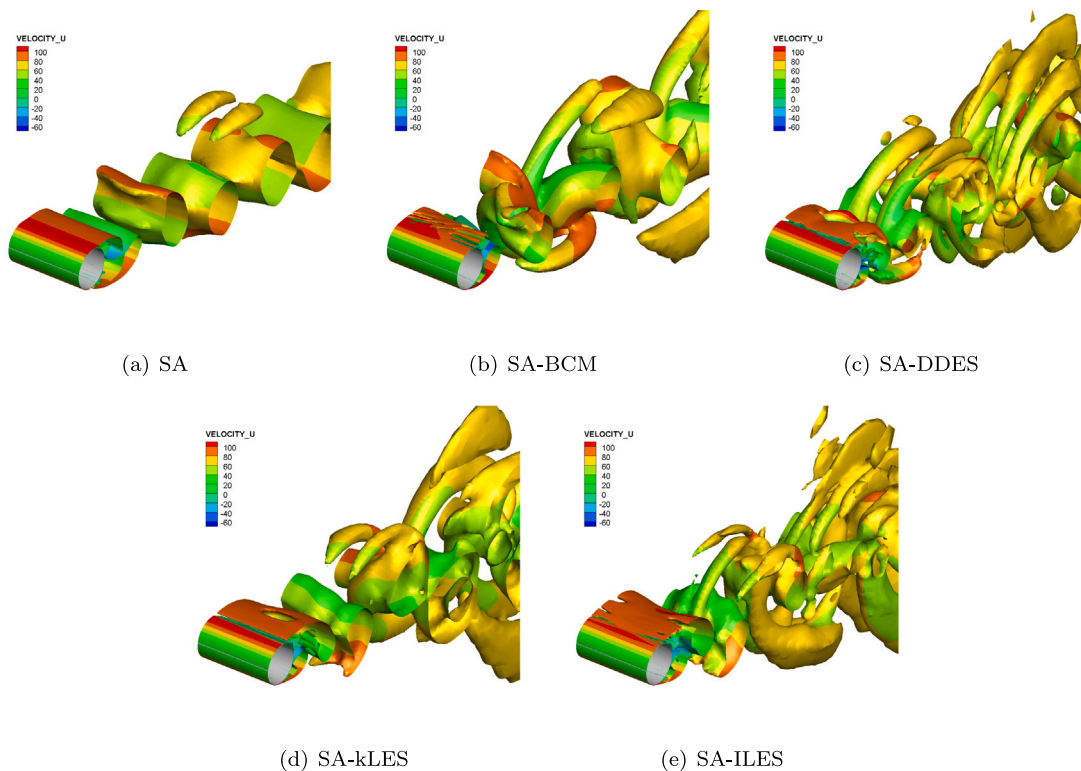
(c) SA-DDES

(d) SA-kLES

(e) SA-ILES

Fig. 14. Instantaneous velocity contours projected on Q-criterion for $Re = 5 \times 10^4$ ($Q = 0.5$).

However, it is not the case on a finer mesh, as shown in Fig. 8(b) for $Re = 1.4 \times 10^5$.

The time-averaged pressure profiles along the cylinder for $Re = 5 \times 10^4$, 1.4×10^5, 4.15×10^5, and 10^6 are shown in Fig. 15. We compare these with their corresponding experimental Re. The hybrid models all show more pressure recovery and delayed separation compared to the experiment and the SA-BCM URANS model (recall that the "turbulent separation" turbulent initialization is employed, which would delay separation). This has been previously observed by Travin et al. (2000) and Moussaed et al. (2014) also. The pressure distribution results of Travin et al. (2000) for $Re = 1.4 \times 10^5$ had a better match for the "laminar separation" laminar initialization while the turbulent separation had an increased pressure recovery (and thus decreasing the drag coefficient) when compared with the experiments. This was also

observed by Moussaed et al. (2014). Interestingly, the pressure coefficient distribution of the SA-ILES model is different from other hybrid models at these angles, but its pressure recovery is almost identical to those of the SA-DDES and SA-kLES models at all Re considered.

The SA-BCM transition model predictions of C_p are quite different from others. The pressure recovery close to the base of the cylinder is predicted much better than by the other models. For instance, the experimental trends of Cantwell and Coles (1983) for $Re = 1.4 \times 10^5$ are well predicted; the trend of Achenbach (1968) for $Re = 8.5 \times 10^5$ is also captured at the base of the cylinder. As a result, the SA-BCM model performs better than all other models in predicting the base pressure coefficients across the range of Reynolds numbers of the drag-crisis, as seen in Fig. 16. Similarly, in terms of the $\overline{C_d}$, the SA-BCM model seems to be the only model that captures the drag crisis as shown in Fig. 17. It is worth noting that grids employed in the LES simulations (Rodríguez
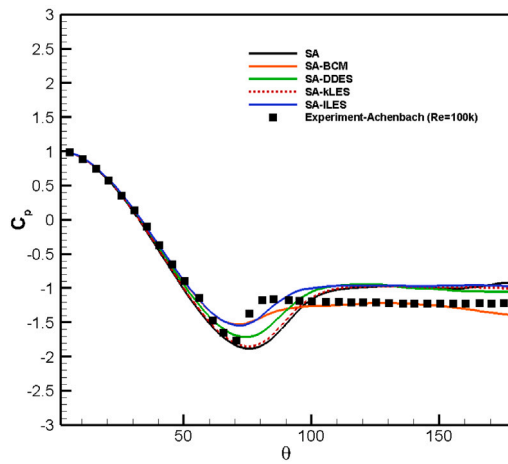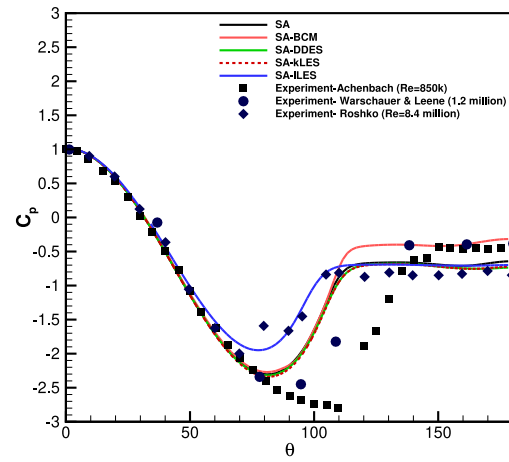
(a) $Re = 5 \times 10^4$
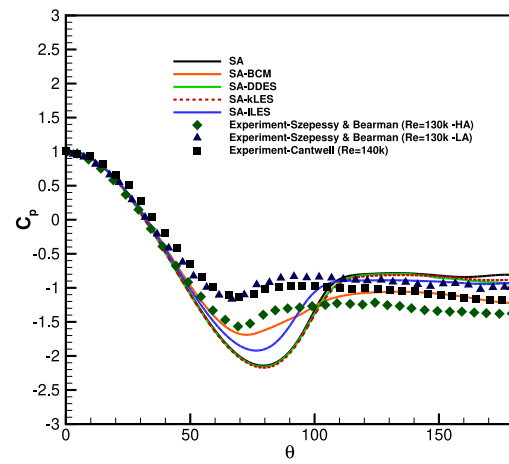
(b) $Re = 1.4 \times 10^5$
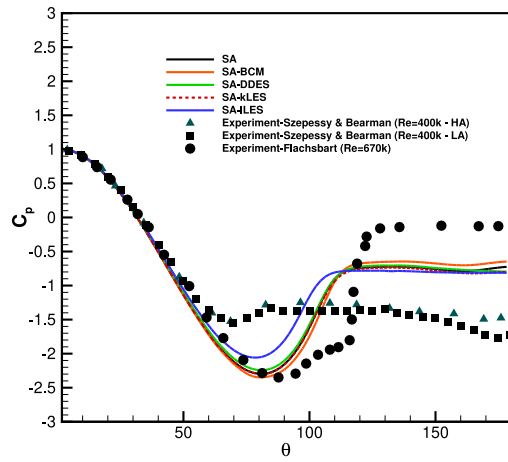
(c) $Re = 4.15 \times 10^5$

(d) $Re = 10^6$

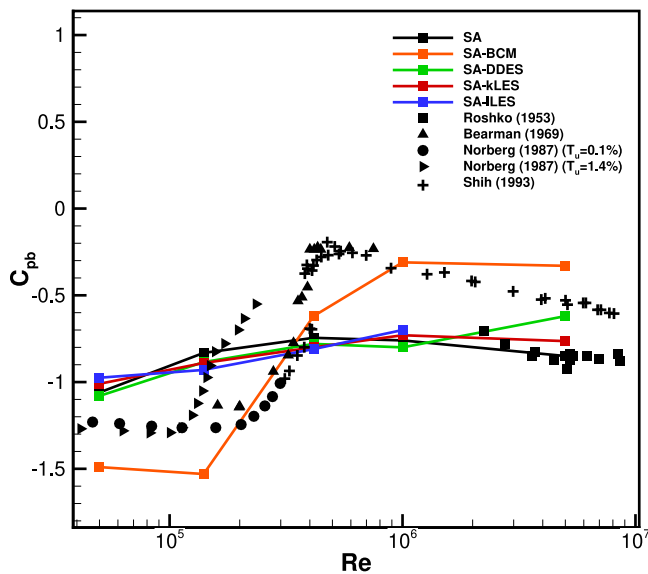**Fig. 15.** Pressure distribution along the cylinder surface.

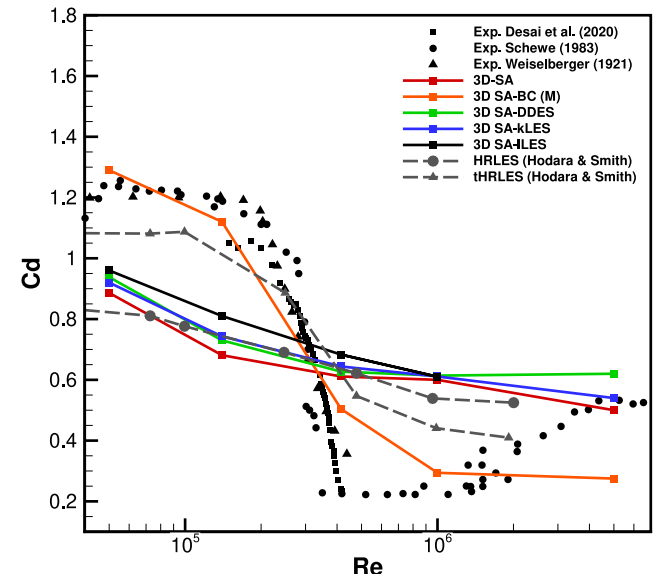**Fig. 16.** Base pressure coefficient C_{pb} variation w.r.t the Reynolds number Re.

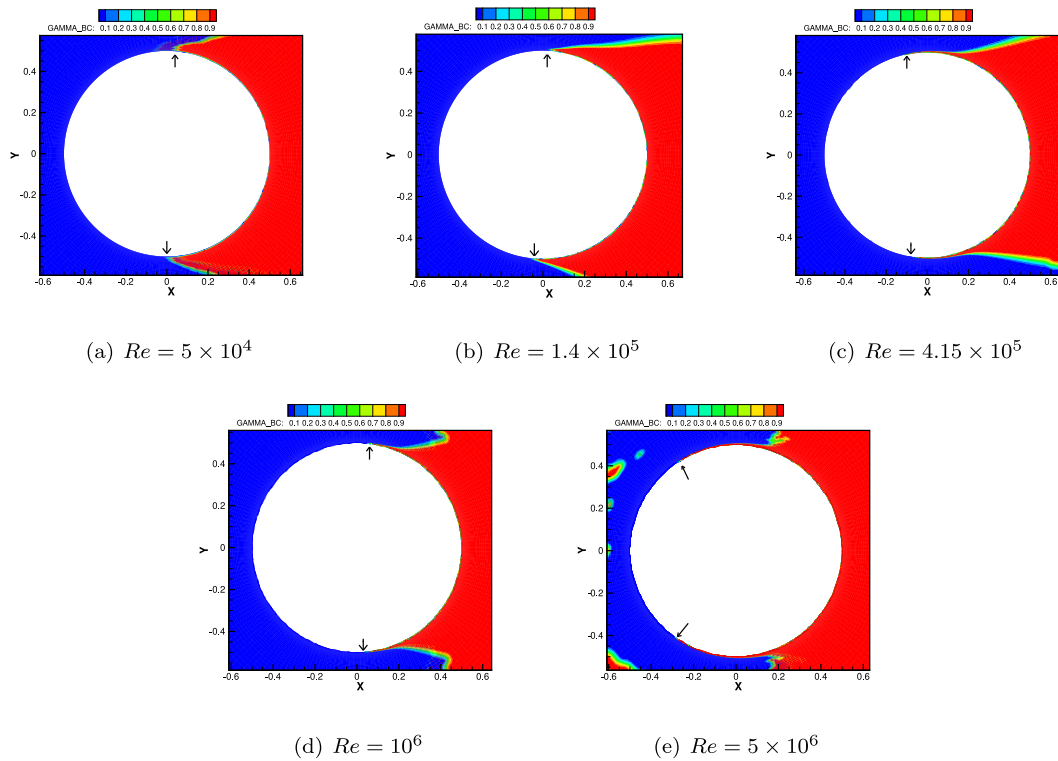**Fig. 17.** Drag coefficient $\overline{C_d}$ variation w.r.t the Reynolds number Re.

(a) $Re = 5 \times 10^4$

(b) $Re = 1.4 \times 10^5$

(c) $Re = 4.15 \times 10^5$

(d) $Re = 10^6$

(e) $Re = 5 \times 10^6$

Fig. 18. γ_{BC} contours of the transition model; Red region indicates the turbulent region and blue one indicates laminar region. The arrows indicate the start of the turbulent boundary layer (as observed directly in the figures after magnification).
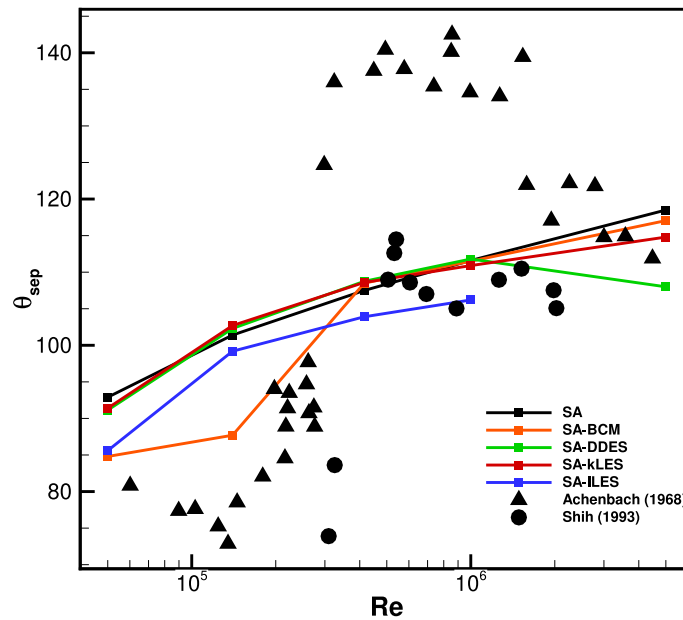

Fig. 19. Variation of separation angle with change in Reynolds number.

et al., 2015; Yeon et al., 2016) that also captured the drag crisis (see Fig. 1) had cells varying from 38 million to 100 million, whereas, in the present study, the grids used have at most 1 million cells. For all the other models, there is a decline in the drag coefficient, but it is a smooth decline rather than a sharp decline like that of the experiments and the SA-BCM. The reason for this can be attributed to the boundary layer transition, which none of the models except SA-BCM take into account.

We have the data of the hybrid RANS-LES (HRLES) and transition hybrid RANS-LES (tHRLES) results of Hodara and Smith (2017) in

Fig. 17 for the sake of comparison. It is noteworthy that the hybrid model gives almost identical results to the present models of this study, while the transition model does better in predicting the drag crisis. This enforces our study's conclusion that transition effects are very important in this problem and must be incorporated into hybrid RANS-LES models used for bluff bodies in mid-range Reynolds numbers.

Beyond the drag crisis, however, the drag coefficients obtained from the SA, SA-DDES, and SA-kLES models at the trans-critical $Re = 5 \times 10^6$ matched well with the experiments, while SA-BCM under-predicted the drag values. Due to the boundary layer being turbulent at
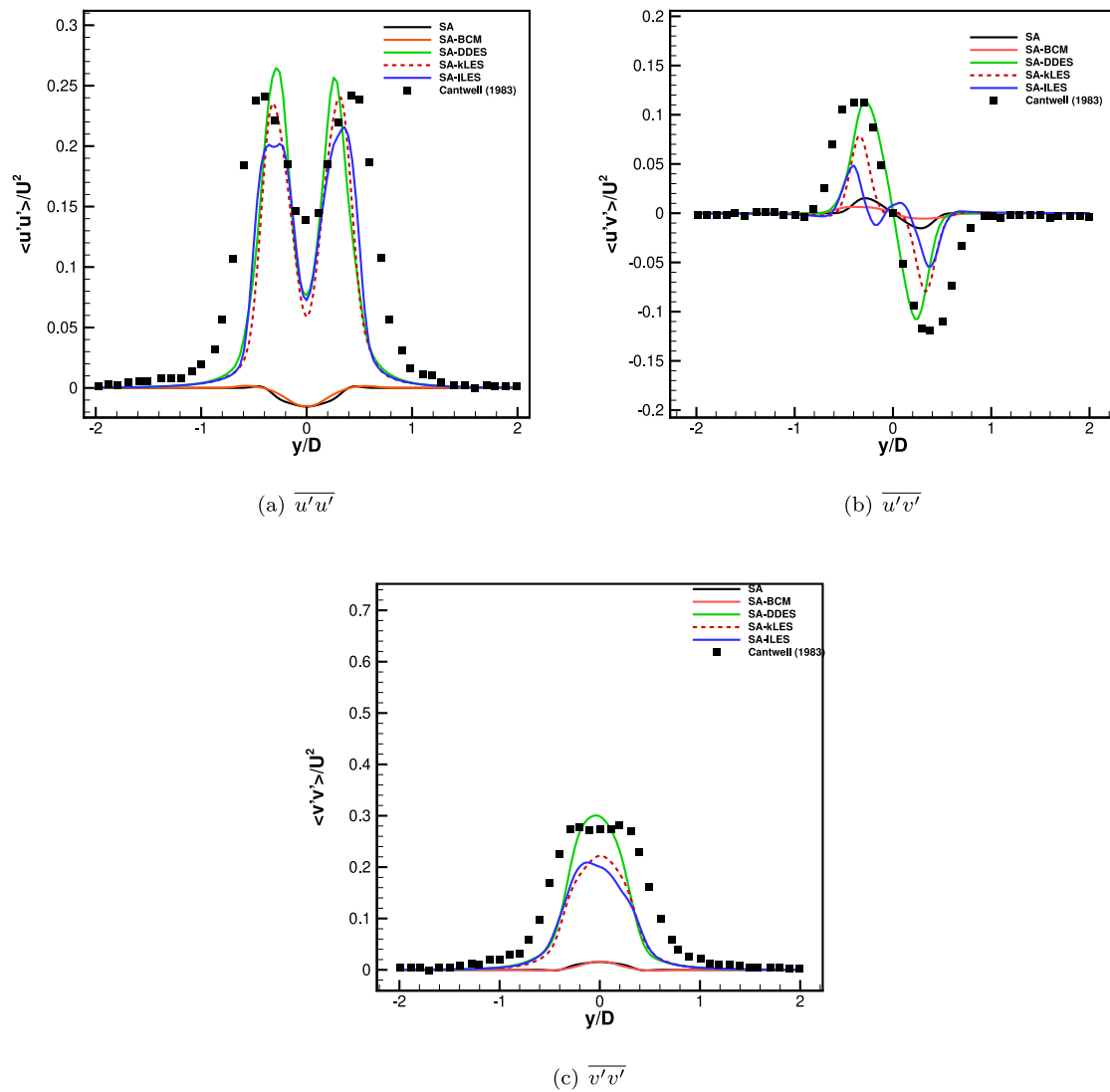
(a) $\overline{u'u'}$

(b) $\overline{u'v'}$

(c) $\overline{v'v'}$

Fig. 20. Comparison of resolved Reynolds stresses of hybrid models and modeled Reynolds stresses of URANS models with the experiments for $Re = 1.4 \times 10^5$ in the wake region ($x/d = 1$). Refer to Appendix for the averaging procedure.

this trans-critical Re, the SA, SA-DDES, and SA-kLES performed better than the SA-BCM transition model. The effect of transition modeling in SA-BCM can be directly seen. The time-averaged contours of the intermittency function (γ_{BC}) of the SA-BCM model are shown in Fig. 18. The function γ_{BC} effectively checks for the experimental momentum thickness Reynolds number and activates the turbulent production term if it reaches the threshold. The red region depicts the presence of turbulent activity, and the blue one indicates its absence. The contours suggest that the wake is turbulent and the cylinder surface is laminar for Reynolds numbers 5×10^4 and 1.4×10^5, with the boundary layer becoming turbulent earlier as Re is increased.

The separation angle (θ_S) is also better predicted (see Fig. 19) by the SA-BCM model compared to the other models. For example, θ_S is least for $Re = 5 \times 10^4$ and 1.4×10^5 with almost the same angle, beyond which there is a sudden increase due to turbulent boundary layer transition, as can be seen from Fig. 19. The other models, however, predicted a higher θ_S by around 15 degrees at $Re = 5 \times 10^4$ and 1.4×10^5 due to the fully turbulent boundary layer assumed there.

The frequency of vortex shedding should be higher after turbulent boundary layer transition. This is evident from the experimental data and is also seen in the LES study of Rodríguez et al. (2015). The Strouhal number (St) for various models is shown in Table 6. For the sub-critical $Re = 1.4 \times 10^5$ and the supercritical $Re = 10^6$, the St

prediction of SA-BCM is superior to other models. The reason for this can be attributed to a better prediction of the separation angle. The separation angle predicted by the SA-BCM model at $Re = 1.4 \times 10^5$ is close to 87 degrees (compared to the experimental value of 80 degrees Achenbach, 1968), whereas other models predicted around 100 degrees. Hence a significant difference in St can be seen in this case. For Re of 1 million, none of the models predicted the exact experimental St, with SA-BCM being the closest.

The comparison of Reynolds stresses, computed for $Re = 1.4 \times 10^5$, one diameter downstream of the rear stagnation point with the experiments of Cantwell and Coles (1983), for the same Re, are shown in Fig. 20. The averaging procedure followed to obtain the Reynolds shear stresses is given in Appendix. It is seen that the SA-BCM and SA poorly predict the form and peak of $\overline{u'u'}$, $\overline{u'v'}$ and $\overline{v'v'}$, while the predictions of all three hybrid models are quite good.

This suggests that the RANS-LES hybrid models do capture the turbulent flow field well and better than the RANS models, but only where the flow field is actually turbulent, i.e., not complicated by laminar–turbulent transition, etc. This is encouraging, as hybrid models are seen as the future of turbulence modeling for practical engineering flows. But it also suggests that it is important that hybrid models are equipped to handle the laminar–turbulent transition to become robust tools for such simulations.

Table 6
Strouhal number comparison with experiments.

Re	Exp. Roshko (1954)	Exp. Bearman (1969)	SA	SA-BCM	SA-DDES	SA-kLES	SA-ILES
1.4×10^5	0.19	0.185	0.256	0.199	0.258	0.259	0.246
10^6	0.38	0.43	0.271	0.31	0.27	0.265	0.26

7. Conclusion

In the present study, we simulated the drag crisis problem for *Re* 50,000 to 5 million with two URANS models: the SA model and the SA-BCM transition model, and with three hybrid RANS-LES models, namely, the SA-DDES, SA-kLES, SA-ILES models. All the models were implemented in an in-house solver with a second-order method. The hybrid models and the SA model are simulated with turbulent initiation, while the SA-BCM model is initiated with free-stream turbulence of 0.4%. A grid sensitivity study was performed with the SA-DDES model. The study on the effect of hybrid models (SA-DDES, SA-kLES. SA-ILES), which are very different LES models, surprisingly, gave quite similar results for the problem. Further comparative study of the models is warranted.

The drag crisis simulations were performed with grids that resolve 80% turbulent kinetic energy, as recommended for LES studies. The URANS transition SA-BCM model best predicted the experimental trend of drag coefficients, base pressure coefficients, and separation angles for the Reynolds numbers studied except in the trans-critical (5×10^6) regime, where the hybrid RANS-LES models did better. Only the SA-BCM model could be said to have captured the drag crisis, and it did this as well as the best LES studies. The hybrid RANS-LES models could not predict the sharp transition of $\overline{C_d}$ at the drag crisis but rather gave a smooth decline of $\overline{C_d}$.

In the wake region, however, the hybrid RANS-LES models gave better predictions of the Reynolds stresses than the two URANS models. They also showed typically turbulence-like behavior, based on the Q-criterion, compared to URANS models.

The overall performance of the SA-BCM model in comparison to the hybrid RANS-LES models is strikingly better for drag crisis Reynolds numbers, apparently due to the prediction of laminar–turbulent transition. However, this should not be viewed as a failure of the hybrid models; rather, the hybrid models should be combined with the transition models to get the best out of both for accurately predicting complex flows involving transition and separation features.

This study suggests that while the drag crisis is better captured by the transition model, the hybrid RANS-LES models better capture the turbulence in the wake. This underlines the role of laminar to turbulent transition for the critical regime Reynolds numbers of the drag crisis and encourages us to include transitional features in the hybrid models to exploit the best of both. It would suggest that the performance of the hybrid RANS-LES models in regions of flow separation could be improved if there is more focus on the laminar–turbulent transition in these models.

To summarize other key findings, the SA-kLES and SA-ILES models performed on par with the DDES model and gave results similar to the latter. This warrants further study in future work.

CRediT authorship contribution statement

Sai Saketha Chandra Athkuri: Methodology, Visualization, Validation, Writing – original draft. **M.R. Nived:** Software, Writing – review & editing. **R. Aswin:** Formal analysis, Investigation. **Vinayak Eswaran:** Conceptualization, Supervision, Resources, Funding acquisition, Writing – review & editing.

Declaration of competing interest

The authors declare that they have no known competing financial interests or personal relationships that could have appeared to influence the work reported in this paper.

Data availability

No data was used for the research described in the article.

Appendix. Averaging analysis

In this section, we briefly describe the averaging procedure performed on the hybrid RANS-LES simulation data. The instantaneous velocity vector is split into two components, namely, the time-averaged and fluctuating components (here bar denotes the time-averaged component, and the prime denotes the fluctuating component):

$$u_i = \bar{u}_i + u'_i. \tag{A.1}$$

The averaged quantity $\bar{u}_i$ is obtained by performing a time-averaging operation over 200-time units. Similarly, the fluctuating part u'_i by subtracting the time-averaged component from the instantaneous field.

$$u'_i = u_i - \bar{u}_i. \tag{A.2}$$

The resolved Reynolds stress tensor $\mathcal{R}_{ij}$ per unit density is computed by performing a time averaging operation on term $u'_i u'_j$.

$$\frac{\mathcal{R}_{ij}}{\rho} = \begin{pmatrix} \overline{u'u'} & \overline{u'v'} & \overline{u'w'} \\ \overline{v'u'} & \overline{v'v'} & \overline{v'w'} \\ \overline{w'u'} & \overline{w'v'} & \overline{w'w'} \end{pmatrix} \tag{A.3}$$

The modeled Reynolds stress tensor for a URANS model is obtained from its turbulent viscosity.

$$\overline{u'_i u'_j} = -\frac{\tau_{ij}}{\rho}. \tag{A.4}$$

where the shear stress τ_{ij} is given as:

$$\tau_{ij} = 2\mu_t \left(\bar{S}_{ij} - \frac{1}{3} \frac{\partial \bar{u}_k}{\partial x_k} \right). \tag{A.5}$$

References

Achenbach, E., 1968. Distribution of local pressure and skin friction around a circular cylinder in cross-flow up to Re=5*10⁶. J. Fluid Mech. 34, 625–639. http://dx.doi.org/10.1017/S0022112068002120.

Assam, A., Narayan Kalkote, N., Sharma, V., Eswaran, V., 2018. An automatic wall treatment for Spalart–Allmaras turbulence model. J. Fluids Eng. 140 (6), 061403. http://dx.doi.org/10.1115/1.4039087.

Athkuri, S.S.C., Eswaran, V., 2020. A new auxiliary volume-based gradient algorithm for tri and tetrahedral meshes. J. Comput. Phys. 422, 109780. http://dx.doi.org/10.1016/j.jcp.2020.109780, URL: https://www.sciencedirect.com/science/article/pii/S0021999120305544?via%3Dihub.

Athkuri, S.S.C., Nived, M.R., Eswaran, V., 2022. The mid-point Green-Gauss gradient method and its efficient implementation in a 3D unstructured finite volume solver. Internat. J. Numer. Methods Fluids 94 (5), 395–422. http://dx.doi.org/10.1002/fld.5059, URL: https://onlinelibrary.wiley.com/doi/full/10.1002/fld.5059.

Bearman, P.W., 1969. On vortex shedding from a circular cylinder in the critical Reynolds number régime. J. Fluid Mech. 37 (3), 577–585. http://dx.doi.org/10.1017/S0022112069000735.

Blazek, J., 2015. Computational Fluid Dynamics: Principles and Applications. Elsevier, pp. 1–447. http://dx.doi.org/10.1016/C2013-0-19038-1, URL: https://www.elsevier.com/books/computational-fluid-dynamics/blazek/978-0-08-099995-1.

Breuer, M., 2000. A challenging test case for large eddy simulation: high Reynolds number circular cylinder flow. Int. J. Heat Fluid Flow 21 (5), 648–654. http://dx.doi.org/10.1016/S0142-727X(00)00056-4, URL: http://www.sciencedirect.com/science/article/pii/S0142727X00000564, Turbulence and Shear Flow Phenomena 1.

Cakmakcioglu, S.C., Bas, O., Kaynak, U., 2018. A correlation-based algebraic transition model. Proc. Inst. Mech. Eng. C 232 (21), 3915–3929. http://dx.doi.org/10.1177/0954406217743537.

Çakmakçıoğlu, S.Ç., Baş, O., Mura, R., Kaynak, Ü., 2020. A revised one-equation transitional model for external aerodynamics. In: Aiaa Aviation 2020 Forum, Vol. 1 PartF. American Institute of Aeronautics and Astronautics Inc, AIAA, http://dx.doi.org/10.2514/6.2020-2706, URL: https://arc.aiaa.org/doi/abs/10.2514/6.2020-2706.

Cantwell, B., Coles, D., 1983. An experimental study of entrainment and transport in the turbulent near wake of a circular cylinder. J. Fluid Mech. 136, 321–374. http://dx.doi.org/10.1017/S0022112083002189.

Carati, D., Rogers, M.M., Wray, A.A., 2002. Statistical ensemble of largeeddy simulations. J. Fluid Mech. 455, 195–212. http://dx.doi.org/10.1017/S0022112001007467, URL: https://www.cambridge.org/core/journals/journal-of-fluid-mechanics/article/statistical-ensemble-of-largeeddy-simulations/0E54C9F0A09FB04FCC13C09C41C83C89.

Catalano, P., Wang, M., Iaccarino, G., Moin, P., 2003. Numerical simulation of the flow around a circular cylinder at high Reynolds numbers. Int. J. Heat Fluid Flow 24 (4), 463–469. http://dx.doi.org/10.1016/S0142-727X(03)00061-4, URL: http://www.sciencedirect.com/science/article/pii/S0142727X03000614, Selected Papers from the Fifth International Conference on Engineering Turbulence Modelling and Measurements.

Chandra, A.S.S., 2022. Towards The Development of Transition Hybrid RANS-LES Models (Ph.D. thesis). Indian Institute of Technology Hyderabad, URL: http://raiith.library.iith.ac.in/handle/123456789/12907.

Choi A N, H., Moin, D.P., 2011. Grid-Point Requirements for Large Eddy Simulation: Chapman's Estimates Revisited. Technical Report.

De Langhe, C., Merci, B., Dick, E., 2005a. Hybrid RANS/LES modelling with an approximate renormalization group. I: Model development. J. Turbul. 6, http://dx.doi.org/10.1080/14685240500149781.

De Langhe, C., Merci, B., Lodefier, K., Dick, E., 2005b. Hybrid RANS/LES modelling with an approximate renormalization group. II: Applications. J. Turbul. 6, http://dx.doi.org/10.1080/14685240500149765.

Desai, A., Mittal, S., Mittal, S., 2020. Experimental investigation of vortex shedding past a circular cylinder in the high subcritical regime. Phys. Fluids 32 (1), 014105. http://dx.doi.org/10.1063/1.5124168, URL: http://aip.scitation.org/doi/10.1063/1.5124168.

Eça, L., Hoekstra, M., Hay, A., Pelletier, D., 2007. A manufactured solution for a two-dimensional steady wall-bounded incompressible turbulent flow. Int. J. Comput. Fluid Dyn. 21 (3–4), 175–188. http://dx.doi.org/10.1080/10618560701553436, arXiv:https://doi.org/10.1080/10618560701553436.

Farell, C., Blessmann, J., 1983. On critical flow around smooth circular cylinders. J. Fluid Mech. 136, 375–391. http://dx.doi.org/10.1017/S0022112083002190.

Germano, M., Piomelli, U., Moin, P., Cabot, W.H., 1991. A dynamic subgrid-scale eddy viscosity model. Phys. Fluids A: Fluid Dyn. 3 (7), 1760–1765. http://dx.doi.org/10.1063/1.857955.

Hodara, J., Smith, M.J., 2017. Hybrid Reynolds-averaged Navier–Stokes/large-eddy simulation closure for separated transitional flows. http://dx.doi.org/10.2514/1.J055475, URL: https://arc.aiaa.org/doi/abs/10.2514/1.J055475.

Islam, A., Thornber, B., 2016. Development and Application of a novel RANS and Implicit les Hybrid Turbulence Model for Automotive Aerodynamics. SAE Technical Papers 2016-April, SAE International, http://dx.doi.org/10.4271/2016-01-1608.

James, W.D., Paris, S.W., Malcolm, G.N., 1980. Study of viscous crossflow effects on circular cylinders at high reynolds numbers. AIAA J. 18 (9), 1066–1072. http://dx.doi.org/10.2514/3.50855.

Joshi, A., Assam, A., Nived, M.R., Eswaran, V., 2019. A generalised wall function including compressibility and pressure-gradient terms for the Spalart–Allmaras turbulence model. J. Turbul. 20 (10), 626–660. http://dx.doi.org/10.1080/14685248.2019.1691730, arXiv:https://doi.org/10.1080/14685248.2019.1691730.

Kim, S.E., 2006. Large eddy simulation of turbulent flow past a circular cylinder in subcritical regime. In: Collection of Technical Papers - 44th AIAA Aerospace Sciences Meeting, Vol. 22. American Institute of Aeronautics and Astronautics Inc., pp. 17076–17092. http://dx.doi.org/10.2514/6.2006-1418, URL: https://arc.aiaa.org/doi/abs/10.2514/6.2006-1418.

Lakshmipathy, S., Girimaji, S.S., 2010. Partially averaged Navier-Stokes (PANS) method for turbulence simulations: Flow past a circular cylinder. J. Fluids Eng. Trans. ASME 132 (12), http://dx.doi.org/10.1115/1.4003154.

Lakshmipathy, S., Togiti, V., 2011. Assessment of alternative formulations for the specific-dissipation rate in rans and variable-resolution turbulence models. In: 20th AIAA Computational Fluid Dynamics Conference 2011. American Institute of Aeronautics and Astronautics Inc, http://dx.doi.org/10.2514/6.2011-3978, URL: https://arc.aiaa.org/doi/abs/10.2514/6.2011-3978.

Lee, K., Yang, K.S., 2017. Large eddy simulation of turbulent flow past a circular cylinder in the subcritical and critical regimes. J. Mech. Sci. Technol. 31 (4), 1729–1737. http://dx.doi.org/10.1007/s12206-017-0321-z, URL: https://link.springer.com/article/10.1007/s12206-017-0321-z.

Lilly, D.K., 1992. A proposed modification of the germano subgrid-scale closure method. Phys. Fluids A 4 (3), 633–635. http://dx.doi.org/10.1063/1.858280.

Lloyd, T.P., James, M., 2016. Large eddy simulations of a circular cylinder at Reynolds numbers surrounding the drag crisis. Appl. Ocean Res. 59, 676–686. http://dx.doi.org/10.1016/j.apor.2015.11.009, URL: http://www.sciencedirect.com/science/article/pii/S0141118715001510.

Lo, S.-C., Hoffmann, K.A., Dietiker, J.-F., 2005. Numerical investigation of high Reynolds number flows over square and circular cylinders. J. Thermophys. Heat Transfer 19, 72–80. http://dx.doi.org/10.2514/1.9195, URL: https://arc.aiaa.org/doi/10.2514/1.9195.

Moussaed, C., Vittoria Salvetti, M., Wornom, S., Koobus, B., Dervieux, A., 2014. Simulation of the flow past a circular cylinder in the supercritical regime by blending RANS and variational-multiscale LES models. J. Fluids Struct. 47, 114–123. http://dx.doi.org/10.1016/j.jfluidstructs.2013.11.006, URL: http://www.sciencedirect.com/science/article/pii/S0889974613002508, Special Issue on Unsteady Separation in Fluid-Structure Interaction-l.

Nived, M., Athkuri, S.S.C., Eswaran, V., 2022. On the application of higher-order backward difference (BDF) methods for computing turbulent flows. Comput. Math. Appl. 117, 299–311. http://dx.doi.org/10.1016/j.camwa.2022.05.007, URL: https://www.sciencedirect.com/science/article/pii/S0898122122001948.

Pereira, F., Vaz, G., Eça, L., Girimaji, S., 2018. Simulation of the flow around a circular cylinder at re=3900 with partially-averaged Navier-Stokes equations. Int. J. Heat Fluid Flow 69, 234–246. http://dx.doi.org/10.1016/j.ijheatfluidflow.2017.11.001, URL: http://www.sciencedirect.com/science/article/pii/S0142727X16309377.

Perrin, R., Braza, M., Cid, E., Cazin, S., Barthet, A., Sevrain, A., Mockett, C., Thiele, F., 2007. Obtaining phase averaged turbulence properties in the near wake of a circular cylinder at high Reynolds number using POD. Exp. Fluids 43 (2), 341–355. http://dx.doi.org/10.1007/s00348-007-0347-6.

Perrin, R., Mockett, C., Braza, M., Cid, E., Cazin, S., Sevrain, A., Chassaing, P., Thiele, F., 2008. Joint numerical and experimental investigation of the flow around a circular cylinder at high Reynolds number. In: Particle Image Velocimetry: New Developments and Recent Applications. Springer Berlin Heidelberg, Berlin, Heidelberg, pp. 223–244. http://dx.doi.org/10.1007/978-3-540-73528-1_11.

Pfeil, H., Orth, U., 1990. Boundary-layer transition on a cylinder with and without separation bubbles. Exp. Fluids 10 (1), 23–32. http://dx.doi.org/10.1007/BF00187868, URL: https://link.springer.com/article/10.1007/BF00187868.

Pope, S.B., 2001. Turbulent flows. Meas. Sci. Technol. 12 (11), 2020–2021. http://dx.doi.org/10.1088/0957-0233/12/11/705, arXiv:arXiv:1011.1669v3 URL: http://stacks.iop.org/0957-0233/12/i=11/a=705?key=crossref.71804963fd6eca6048b82cb2b9527350.

Resource, T.M., 2021. NASA langley research center. https://turbmodels.larc.nasa.gov/ [Accessed: 2021-07-30].

Rodríguez, I., Lehmkuhl, O., Chiva, J., Borrell, R., Oliva, A., 2015. On the flow past a circular cylinder from critical to super-critical Reynolds numbers: Wake topology and vortex shedding. Int. J. Heat Fluid Flow 55, 91–103. http://dx.doi.org/10.1016/j.ijheatfluidflow.2015.05.009, URL: http://www.sciencedirect.com/science/article/pii/S0142727X15000557, Special Issue devoted to the 10th Int. Symposium on Engineering Turbulence Modelling and Measurements (ETMM10) held in Marbella, Spain on September 17-19, 2014.

Roshko, 1954. On the Drag and Shedding Frequency of Two-Dimensional Bluff Bodies. NACA Technical Note 3169.

Roshko, A., 1961. Experiments on the flow past a circular cylinder at very high Reynolds number. J. Fluid Mech. 10 (3), 345–356. http://dx.doi.org/10.1017/S0022112061000950.

Sagaut, P., 2006. Large Eddy Simulation for Incompressible Flows. In: Scientific Computation, Springer-Verlag, Berlin/Heidelberg, http://dx.doi.org/10.1007/b137536, URL: http://link.springer.com/10.1007/b137536.

Savill, A., 1993. Some Recent Progress in Turbulence Modeling of By-pass Transition. Elsevier, pp. 829–848.

Schewe, G., 1983. On the force fluctuations acting on a circular cylinder in crossflow from subcritical up to transcritical Reynolds numbers. J. Fluid Mech. 133, 265–285. http://dx.doi.org/10.1017/S0022112083001913.

Schubauer, G.B., Klebanoff, P.S., 1955. Contributions on the mechanics of boundary-layer transition. URL: https://ntrs.nasa.gov/citations/19930092285.

Shih, W., Wang, C., Coles, D., Roshko, A., 1993. Experiments on flow past rough circular cylinders at large Reynolds numbers. J. Wind Eng. Ind. Aerodyn. 49 (1), 351–368. http://dx.doi.org/10.1016/0167-6105(93)90030-R, URL: http://www.sciencedirect.com/science/article/pii/016761059390030R.

Shur, M.L., Spalart, P.R., Strelets, M.K., Travin, A.K., 2015. An enhanced version of DES with rapid transition from RANS to LES in separated flows. Flow Turbul. Combust. 95 (4), 709–737. http://dx.doi.org/10.1007/S10494-015-9618-0, URL: https://link.springer.com/article/10.1007/s10494-015-9618-0.

Singh, S.P., Mittal, S., 2005. Flow past a cylinder: shear layer instability and drag crisis. Internat. J. Numer. Methods Fluids 47 (1), 75–98. http://dx.doi.org/10.1002/fld.807, URL: http://doi.wiley.com/10.1002/fld.807.

Spalart, P., 1997. Comments on the feasibility of LES for wings, and on a hybrid RANS/LES approach.

Spalart, P.R., Allmaras, S.R., 1994. One-equation turbulence model for aerodynamic flows. Rech. Aerospat. (1), 5–21. http://dx.doi.org/10.2514/6.1992-439.

Spalart, P.R., Deck, S., Shur, M.L., Squires, K.D., Strelets, M.K., Travin, A., 2006. A new version of detached-eddy simulation, resistant to ambiguous grid densities. Theor. Comput. Fluid Dyn. 20 (3), 181–195. http://dx.doi.org/10.1007/s00162-006-0015-0, URL: https://link.springer.com/article/10.1007/s00162-006-0015-0.

Travin, A., Shur, M., Strelets, M., Spalart, P., 2000. Detached-eddy simulations past a circular cylinder. Flow Turbul. Combust. 63 (1), 293–313. http://dx.doi.org/10.1023/A:1009901401183.

Vaz, G., Van Der Wal, R., Mabilat, C., Gallagher, P., 2007. Viscous flow computations on smooth cylinders a detailed numerical study with validation. In: Proceedings of the International Conference on Offshore Mechanics and Arctic Engineering - OMAE, Vol. 3. American Society of Mechanical Engineers Digital Collection, pp. 849–860. http://dx.doi.org/10.1115/OMAE2007-29275.

Versión, Menter, F., 2012. Best practice: Scale-resolving simulations in ANSYS CFD.

Warschauer, K., Leene, J., 1971. Experiments on mean and fluctuating pressures of circular cylinders at cross flow at very high Reynolds numbers. In: Proc. Int. Conf. on Wind Effects on Buildings and Structures. pp. 305–315.

Weiss, J.M., Maruszewski, J.P., Smith, W.A., 1999. Implicit solution of preconditioned Navier-Stokes equations using algebraic multigrid. AIAA J. 37 (1), 29–36. http://dx.doi.org/10.2514/2.689, URL: http://arc.aiaa.org/doi/10.2514/2.689.

Wieselsberger, C., 1922. Weitere feststellungen uber die gesetze des flussigkeits und luftwiderstandes. Phys. Z. 23, 219–224, URL: https://cir.nii.ac.jp/crid/1571698600022304128.

Williamson, C.H.K., 1996. Vortex dynamics in the cylinder wake. Annu. Rev. Fluid Mech. 28 (1), 477–539. http://dx.doi.org/10.1146/annurev.fl.28.010196.002401, arXiv:https://doi.org/10.1146/annurev.fl.28.010196.002401.

Wong, V.C., Lilly, D.K., 1994. A comparison of two dynamic subgrid closure methods for turbulent thermal convection. (ISSN: 10706631) http://dx.doi.org/10.1063/1.868335, URL: http://aip.scitation.org/doi/10.1063/1.868335.

Ye, H., Wan, D., 2017. Benchmark computations for flows around a stationary cylinder with high Reynolds numbers by RANS-overset grid approach. Appl. Ocean Res. 65, 315–326. http://dx.doi.org/10.1016/j.apor.2016.10.010, URL: http://www.sciencedirect.com/science/article/pii/S0141118716304667.

Yeon, S.M., Yang, J., Stern, F., 2016. Large-eddy simulation of the flow past a circular cylinder at sub- to super-critical Reynolds numbers. Appl. Ocean Res. 59, 663–675. http://dx.doi.org/10.1016/j.apor.2015.11.013, URL: http://www.sciencedirect.com/science/article/pii/S0141118715001558.